Chitosan/PLA-loaded Magnesium oxide nanocomposite to attenuate oxidative stress, neuroinflammation, and neurotoxicity in rat models of Alzheimer's disease

Manickam Rajkumar
Periyar University
Govindaraj Prabha
St Joseph's Institute of Technology
Karuppaiya Vimala
Periyar University
Ramasundaram Thangaraj
Periyar University
Soundarapandian Kannan (sk_protein@periyaruniversity.ac.in)
Periyar University https://orcid.org/0000-0002-5388-3746

Research Article

Keywords: Magnesium oxide, Amyloid-β aggregation, Oxidative stress, Neuroinflammation

Posted Date: October 31st, 2023

DOI: https://doi.org/10.21203/rs.3.rs-3474684/v1

Version of Record: A version of this preprint was published at Metabolic Brain Disease on December 12th, 2023. See the published version at https://doi.org/10.1007/s11011-023-01336-x.

Chitosan/PLA-loaded Magnesium oxide nanocomposite to attenuate oxidative stress, neuroinflammation, and neurotoxicity in rat models of Alzheimer's disease

Manickam Rajkumar[1], Prabha Govindaraj[2], Karuppaiya Vimala[1], Ramasundaram Thangaraj[3], Soundarapandian Kannan[1,*]

[1]Cancer Nanomedicine Laboratory, Department of Zoology, School of Life Sciences, Periyar University, Salem-636 011, Tamil Nadu, India

[2]Department of Chemistry, St. Joseph's Institute of Technology, Chennai-636 119, Tamil Nadu, India

[3]Vermitechnology and Ecotoxicology Laboratory, Department of Zoology, School of Life Sciences, Periyar University, Salem-636 011, Tamil Nadu, India

ORCID ID:

Manickam Rajkumar: 0000-0002-4352-6630

Prabha Govindaraj: 0000-0001-7529-9180

Karuppaiya Vimala: 0000-0002-6273-4136

Ramasundaram Thangaraj: 0000-0002-6374-5160

Soundrapandian Kannan*: 0000-0002-0583-2530

[*]**Corresponding author**

Prof. S. Kannan,

Cancer Nanomedicine, Department of Zoology, School of Life Sciences, Periyar University, Salem-636 011, Tamil Nadu, India

Tel: +91 9585132032

Email: sk_protein@periyaruniversity.ac.in

Abstract

Alzheimer's disease (AD) is a neurodegenerative disease characterized by amyloid-beta (Aβ) aggregation, neuroinflammation, oxidative stress, and dysfunction in the mitochondria and cholinergic system. In this study, the synthesis of chitosan-polylactic acid-loaded magnesium oxide nanocomposite (CH/PLA/MgONCs) was examined using the green precipitation method. The synthesized CH/PLA/MgONCs were confirmed by using the UV-Vis spectrum, FT-IR, SEM-EDAX, and physical properties. The experiments were carried out using male Wistar rats by injecting streptozotocin (STZ) bilaterally into the brain's ventricles through the intracerebroventricular (ICV) route at a dose of 3 mg/kg. We also evaluated the effects of CH/PLA/MgONCs at doses of 10 mg/kg. To assess the cognitive dysfunction induced by ICV-STZ, we performed behavioral, biochemical, and histopathological analyses. In our study results, UV-Vis spectrum analysis of CH/PLA/MgONCs showed 285 nm, FT-IR analyses confirmed that the various functional groups were present, and SEM-EDAX analysis confirmed that a cauliflower-like spherical shape, Mg and O were present. Treatment with CH/PLA/MgONCs (10 mg/kg) showed a significant improvement in spatial and non-spatial memory functions. This was further supported by biochemical analysis showing improved antioxidant enzyme (GSH, SOD, CAT, and GPx activity) activities that significantly attenuated cholinergic activity and oxidative stress. In the CH/PLA/MgONCs-treated group, significant improvement was observed in the mitochondrial complex activity. ICV-STZ-induced neuroinflammation, as indicated by increased levels of TNF-α, IL-6, and CRP, was significantly reduced by CH/PLA/MgONCs treatment. Additionally, CH/PLA/MgONCs treated histological results showed improved healthy neuronal cells in the brain. Furthermore,

in silico studies confirm that these molecules have good binding affinity and inhibit Aβ aggregation. In conclusion, CH/PLA/MgONCs treatment reversed AD pathology by improving memory and reducing oxidative stress, neuroinflammation, and mitochondrial dysfunction. These findings recommend that CH/PLA/MgONCs are possible therapeutic agents to treat AD.

Keywords: Magnesium oxide, Amyloid-β aggregation, Oxidative stress, Neuroinflammation

1. Introduction

Alzheimer's disease (AD) is a kind of progressive neurodegenerative disorder that is characterized by various pathological features, including increased oxidative stress, loss of neurons and synapses, accumulation of Aβ plaques, and neurofibrillary tangles (Mishra et al., 2023). According to a 2017 report, approximately 44 million people worldwide are currently affected by AD, and this number is projected to rise to 115 million by 2050 (Pan et al., 2021). Several factors have been identified as contributors to the pathology of AD. Oxidative stress occurs when there is an imbalance between pro-oxidants and antioxidants in the body, resulting in the production of harmful reactive oxygen species (ROS). This phenomenon has been linked to the emergence of different neurodegenerative conditions, such as AD (Gaur et al., 2021). The imbalance can occur due to excessive production of free radicals, a decrease in the body's antioxidant defenses, and overproduction of acetylcholinesterase (AChE). The brain is particularly susceptible to oxidative damage due to its high oxygen consumption, abundance of polyunsaturated fatty acids, and relatively low levels of natural antioxidant activity compared to other tissues (Ucar et al., 2022; Mishra et al., 2023). Importantly, these phenomena are closely interconnected. This highlights the complex and interconnected nature of the various pathological mechanisms involved in AD. Although some therapeutic targets and interventions have been identified, AD still poses a significant medical challenge.

Despite more than three decades of extensive research, there is still no consensus on the causes and mechanisms of AD, the most common form of the disease. Furthermore, the prevalence of AD is rapidly increasing, highlighting the urgent need for more effective therapies to address this growing public health concern (Penney et al., 2020).

The field of nanotechnology has undergone a revolutionary transformation in the design and development of potential drug delivery systems (DDS) that can minimize toxic (Sahu et al., 2021). Nanoparticulate (NPs) drug delivery offers a promising approach to enhancing the transport of drugs through physiological barriers like the blood-brain barrier (BBB). Due to their small size, customized surface characteristics, improved solubility, multifunctionality, prolonged circulation, and targeted accumulation at specific sites, nanoparticles have the potential to interact with cellular functions in novel ways (Mitchell et al., 2021). In recent years, researchers have shown significant interest in metal oxide nanoparticles that are coated with bio-organic polymers or ligands, primarily due to their wide range of pharmaceutical and biomedical applications. The surface modification of these metal oxide nanoparticles with organic polymers can greatly enhance their physical, chemical, and biological properties (Okolie et al., 2021; Sahu et al., 2021).

Coffee arabica (L.), a member of the Rubiaceae family, is a plant used to make coffee and is popular throughout the world. The *Coffee arabica* (CA) plant contains high amounts of hydroxycinnamic acids, caffeic, and ferulic acids (Da Matta et al., 1999; Fernandez et al., 2009). The phenolic acids, polyphenols, and alkaloids in green coffee beans have beneficial phytooxidant activities (Duangzhai et al., 2016). It has high antioxidants and is well recognized as a potential protective factor against human chronic degenerative diseases such as cancer and cardiovascular disease (De Lorenzo et al., 2017). Also, CA exhibits antibacterial activity (Thand et al., 2016), nitrate reductase activity (Da Matta et al., 1999),

antifungal activity (Fernandez et al., 2009), antioxidant and anti-tyrosinacetate activity (Siachinset et al., 2016), and various clinical applications such as neuraminidase inhibitory activity (Muchtaridi et al., 2021).

Chitosan (CS) shows promise as a polymer for developing biodegradable and biocompatible nanoparticles (Islam et al., 2020). Chitosan and polylactic acid (PLA) have garnered particular attention due to their exceptional characteristics, including low toxicity, biodegradability, and biocompatibility (Alhodieb et al., 2022). By conjugating chitosan with metal oxide nanoparticles, surface modifications can significantly improve biocompatibility and biomedical properties. The surface coating of metal oxide nanoparticles, specifically magnesium oxide nanoparticles (MgONPs), with chitosan, has attracted considerable interest due to its versatile applications in biomedicine, catalysis, and degradation (Silva et al., 2022). The combination of chitosan and MgONPs forms a novel generation of biopolymeric nanocomposites. Recent studies have demonstrated that chitosan-coated biopolymeric nanoparticles exhibit remarkable antibacterial and antifungal properties. The chitosan-coated MgO nanocomposite shows great potential in terms of antioxidant and antimicrobial properties (Oladzadabbasabadi et al., 2020).

Recent advancements in brain-targeted drug delivery agents have paved the way for novel therapeutic approaches in the field of neuroscience. Various nano-agents or nano-drugs, including small-molecule drugs and peptide mimetics, have demonstrated effectiveness in inhibiting Aβ aggregation and providing significant neuroprotection (Gong et al., 2021). However, despite these promising developments, clinical trials in this area have faced challenges as many of these agents are unable to penetrate the BBB and lack specific targeting capabilities (Liu et al., 2023). Currently, Aβ inhibitors are of great scientific significance due to their remarkable ability to traverse biological BBB barriers, thus

enhancing their overall therapeutic effectiveness. Considering the aforementioned challenges, there is a strong need to develop innovative nanotherapeutics that exhibit high BBB permeability to optimize the treatment of AD (Ni et al., 2022; Oladzadabbasabadi et al., 2020).

The novelty of the present study is the synthesis of CH/PLA/MgONCs and their investigation in ICV-STZ-induced AD model. In our study, CH/PLA/MgONCs synthesis and its characterization properties were analyzed. Then, the experimental rats were induced with AD by using ICV-STZ, and the AD models were treated with CH/PLA/MgONCs. All experimental rats were evaluated through behavioral studies of spatial and spatial memory functions. Further studies were carried out to detect oxidative stress, antioxidants, and mitochondrial complex activity in the cortex and hippocampus regions of experimental rats. Histopathology studies were performed to assess the structural and morphological changes of nerve cells in the brain. Furthermore, the binding affinity and stability of major plant phytochemicals with the Aβ protein were evaluated by molecular docking analysis. This study provides experimental evidence for the potential use of CH/PLA/MgONCs in the context of AD treatment.

Materials and methods

Materials

Chitosan (Type A, porcine skin-derived), polylactic acid, streptozotocin, magnesium nitrite, trichloroacetic acid (TCA), ethylenediaminetetraacetic acid (EDTA), ascorbic acid, tris buffer-HCL, and 2,4-dinitrophenylhydrazine (DNPH) were purchased from Sigma-Aldrich (MS, US). Nitro blue tetrazolium (NBT), Bovine serum albumin (BSA), phosphate-buffer saline (PBS), thiobarbituric acid (TBA), methyl-thiazolyl diphenyl-tetrazolium

bromide (MTT), nicotinamide adenine dinucleotide reduced (NADH), 5,5'-dithiobisnitro benzoic acid (DTNB), oxidized glutathione (GSSG), hydrogen peroxide (H_2O_2) and glutathione (GSH) were obtained from Himedia (Mumbai, India). Analytical-grade chemicals and reagents were used for this study.

Synthesis of *Coffea Arabica* plant extract

Plant leaves of *Coffea Arabica* (CA) were collected from the Yercaud Hills, Salem, Tamil Nadu, India. Fresh CA leaves were washed with deionized water and fragmented into tiny pieces by weight of 5 grams (gm), and the fragmented pieces of CA leaves were boiled in 100 mL of deionized water at 50 °C for 2 hrs and constantly stirred. The leaf extract was filtered with Whatman No. 1 filter paper. Finally, the prepared leaf extract was stored at 4 °C for further use.

Synthesis of CH/PLA/MgONCs

The CH/PLA/MgONCs were created using the method described previously, with slight modifications. Briefly, $Mg(NO_3)_2$ (0.1 M) was dissolved in 100 ml of deionized water and continuously stirred at 60 ℃ for 3 hrs. Chitosan (2% w/v) and PLA (2% w/v) were dissolved separately in PBS for 2 hrs at 50 °C using a magnetic stirrer until completely dissolved. The $MgO(NO_3)_2$ solution of 90 ml and the CA plant extract of 10 ml (9:1 v/v) were added to the conical flask and allowed to react for 2 hrs at 50 °C under a magnetic stirrer (MgONPs). Last, the aqueous MgONPs of 80 ml, the chitosan solution of 10 ml, and the PLA solution of 10 ml (8:1:1 v/v) were mixed in a conical flask under constant stirring at 60 °C for 3 hrs. Furthermore, glacial acetic acid (1% v/v) was added to the magnetic stirring condition. The synthesized compound was centrifuged at 10 min for 10,000*g*, and the pure pellet solution was obtained. The synthesized CH/PLA/MgONCs solution was freeze-dried at -80

°C for 24 hrs, and the solution was lyophilized for 48 hrs to form a dry material, which was then stored at a freezing temperature for further use.

Characterization of CH/PLA/MgONCs

The synthesized CH/PLA/MgONCs were confirmed by using a UV-Vis spectrophotometer (UV-1800 Shimadzu-Japan), and the Fourier transfer infrared (FT-IR) was used in the 4000–400 cm^{-1} range (NEXUS, 470 Bruker Spectrophotometer). A scanning electron microscope with energy dispersive spectroscopy (SEM-EDAX, Carl Zeiss, Germany) was used for surface structure morphology and elemental analysis.

Swelling properties

The swelling properties of CH/PLA/MgONCs were dissolved in PBS and evaluated from 5 min to 24 h at 37 °C. Samples were taken from PBS for cleaning at predefined intervals; surface droplets were removed with tissue paper, weighed, and placed back into PBS. The sample swelling ratio was estimated by the following formula:

$$\text{Swelling ratio } (\%) = \frac{W_t - W_0}{W_0} \times 100$$

Where W_t is the weight of the swollen sample at a particular time point and represents the sample's primary weight of W_0.

***In vitro* drug release study**

The in vitro release of CH, PLA, and MgO from CH/PLA/MgONCs was determined using the dialysis membrane diffusion method. Briefly, a fixed volume of lyophilized NCS suspension was added to a dialysis bag. Then, each dialysis bag containing CH suspension, PLA suspension, and CH/PLA/MgONCs suspension was suspended in a beaker containing 100 ml of phosphate buffer (pH 7.4) with 0.5% tween 80. The mixture was stirred at a

constant speed of 100 rpm and maintained at 37 ± 2 ºC. At predetermined time intervals, samples were collected from the surrounding medium outside the dialysis bag. To ensure sink conditions, the collected medium was promptly substituted with an equivalent volume (0.5 ml) of fresh PBS. The concentrations of CH, PLA, and MgO were measured using a UV spectrophotometer at 446 nm. The experiment was performed in triplicate to ensure the accuracy and reliability of the results (Arduino et al., (2020).

Experimental animals

In this study, we utilized adult male Wistar rats (each group consisted of 6 animals, n = 6). The rats had an average weight of 200 ± 10 gm and were 8 weeks old. The rats were maintained and housed at the Periyar University Central Animal House Facility in Tamil Nadu, and the experimental protocols were approved by the Committee for the Purpose of Control and Supervision of Experiments on Animals (CPCSEA), Government of India, and the Institutional Animal Ethical Committee (PU/IAEC/2020/M1/19) of Periyar University, Tamil Nadu, India. To ensure the well-being of the experimental animals, they were kept in an enclosure with a controlled environment, and standard food and water were provided. The enclosure maintained a continuous temperature of 25 ± 2 °C and a relative humidity of 45–55%. Careful consideration was given to minimizing animal handling, and only a predetermined number of animals were used for the experiment.

Experimental design

The rats were categorized into six distinct groups, each consisting of six animals (n = 6). The groups were designated as follows: Group-I: control group (treated with normal saline); Group-II: ICV-STZ (3 mg/kg); Group-III: STZ+CH (10 mg/kg); Group-IV: STZ+MgO (10 mg/kg); Group-V: STZ+CH/MgO (10 mg/kg); and Group-VI: STZ+CH/PLA/MgONCs (10 mg/kg). To experiment, each rat was anesthetized using an

intraperitoneal (i.p.) injection of ketamine hydrochloride (80 mg/kg/b.w) followed by xylazine (10 mg/kg/b.w). These different drug treatment groups were for 14 days (Fig. 3). Various behavioral studies were conducted from days 16 to 28 to assess the effects of the different drug compounds on the rats. All behavioral assessments were recorded for each group. On the final day of the experiment, all experimental rats were euthanized, and their organs of interest were collected for further analysis. The dissected organs underwent various studies including biochemical, histopathological, and mitochondrial complex activity.

Intracerebroventricular-streptozotocin (ICV-STZ) injection

The STZ was administered in ICV of rats using a stereotaxic apparatus, following the previous method (Paxinos et al., 1980). The rats were anesthetized using ketamine (80 mg/kg, i.p.) and xylazine (10 mg/kg, i.p.). To begin the procedure, the rat's head was shaved and positioned in a stereotaxic apparatus, ensuring that the scalp was tightened and straight. A midline sagittal incision was then made on the scalp using a sharp scalpel blade. Burr holes were drilled on both sides of the skull, directly above the lateral ventricles. The holes were drilled at the following coordinates: 0.8 mm posterior to the bregma, 1.5 mm lateral to the sagittal suture, and 3.6 mm below the cortical surface of the brain. Freshly prepared STZ at a concentration of 3 mg/kg was dissolved in artificial cerebrospinal fluid (CSF) and then injected bilaterally in two divided doses on the first and third days, with each dose being 1.5 mg/kg. The control group of animals received ICV injections of the same volume of CSF. Postoperatively, the rats were provided with glucose water and a normal pellet diet for 4 days, after which they were transitioned to a normal pellet diet alone.

Behavioral assessments

Morris Water Maze (MWM) test

The MWM test, as described in Morris's method (Morris, 1984), was used to assess the learning and spatial memory abilities of the experimental rats. A circular black pool with a diameter of 150 cm and a height of 40 cm was filled with water to a depth of 30 cm. The water was maintained at a temperature of 25 ± 2°C, and its opacity was increased by adding white paint. The experiment included a total of six rats (n = 6). During the experimental period, which spanned from the 16th to the 20th day, each rat underwent training sessions. In each session, the rat was trained five times, starting from four different positions around the border of the maze. Several measures were recorded and calculated to evaluate the rats' performance in the MWM test. Escape latency: The amount of time each rat spent searching for the old platform location. The time each experimental rat spent on the initial part of the platform. Platform crossing time: The time it took for each rat to cross the platform. Travel error times: the number of errors made by each rat during navigation in the maze.

Passive avoidance (PA) test

The PA test was conducted by following the previous method with slight modifications Ramagiri et al., (2017). The experimental setup consisted of two compartments: one that was illuminated and another that was kept dark. Each compartment was equipped with a shock scrambler and a grid platform. These two compartments were separated by a guillotine door. Also, during the acquisition test, each rat was first placed in the lighted box. After a 60-second habituation, the guillotine door separating the lighted and dark rooms was opened. The time it took for the rat to enter the dark compartment, known as the initial latency (IL), was then recorded. Rats whose initial latency period exceeded 60 sec were not included in subsequent experiments. After the rat entered the dark box, an electric shock (50 V, 0.2 mA, 50 Hz) was given for 3 sec on ground phases. After 5 sec, the rat was removed from the dark area and then placed back into its home cage. Retention latency (RL)

duration was measured 24 hrs later using the same procedure as the acquisition test, except that no foot shock was given. The latency time was recorded for a maximum of 300 sec and calculated.

Y-maze test

The Y-maze test was conducted following the previous method to assess non-spatial learning, memory, and cognitive abilities (Conrad et al., 1996). The apparatus used for the test consisted of three arms, each with a length of 50 cm, a height of 15 cm, and a width of 12 cm. These arms were joined together at a 120° angle. The rats were gently placed in the apparatus for 2 min. The total number of times and the order in which they entered the maze were recorded to measure the level of alteration. A higher number of alterations indicated preserved cognition, as it meant that the animals recognized and avoided reentering arms they had previously visited. To quantify the percentage of alternation, the following formula was used:

$$\% \text{ of alternation} = (\text{Actual alternation}/\text{Maximum spontaneous alternation}) \times 100$$

This measurement provided a percentage value indicating the extent of alternation in the rats' behavior during the test.

Biochemical measurements

Dissection and homogenization

After the last behavioral tests, all experimental rats were euthanized, and their brain parts were immediately removed (Sharma et al., 2015). The cortex (CS) and hippocampus (HS) were dissected using a rat brain matrix. To prevent oxidation of the dissected brain tissues, homogenization was performed at a temperature of 4 °C using 10 mM Tris buffer

(pH 7.4) containing protease inhibitors. The protease inhibitors used were 5 mM leupeptin, 1.5 mM aprotinin, 2 mM phenyl methyl sulfonylfluoride (PMSF), 3 mM peptastatin A, 1 mM benzamidine, 10 mM EDTA, 0.1 mM EGTA, and 0.04% butylated hydroxytoluene. Afterwards, the homogenate was centrifuged at 800*g* for 5 min at 4 °C. The resultant supernatant was used to measure TBARS, which is an indicator of oxidative stress. The dissected brain parts were subsequently subjected to processing and analysis through homogenization, centrifugation, and biochemical assays to study oxidative stress and other relevant biochemical markers.

Estimation of AChE activity

The AChE is an important enzyme responsible for breaking down acetylcholine, which serves as a marker for cholinergic neurons in the brain. In this study, the enzyme activity was evaluated in both the CS and HS regions, following the protocol established by Ellman et al. (1961). To measure the activity of AChE, an assay mixture was prepared. This mixture consisted of 50 µl of supernatant, 3 ml of sodium phosphate buffer (pH 8), 0.1 ml of acetylthiocholine iodide, and 0.1 ml of 5,5-dithiobis-2-nitrobenzoic acid (DTNB-Ellman's reagent). The change in absorbance was then monitored for 2 min, with measurements taken at 30-second intervals using a UV-Vis spectrophotometer set to a wavelength of 412 nm. The results obtained were calculated using the molar extinction coefficient of the chromophore, which was determined to be 1.36×10^4 M^{-1} cm^{-1}. The activity of AChE is expressed in nanomoles (nM) of acetylthiocholine iodide hydrolyzed/min/mg of protein.

Estimation of glutathione (GSH) activity

The GSH was assayed following the method described by Jollow et al. (1974). Briefly, 100 µl of the supernatant obtained from tissue homogenate was combined with 1 ml

of 4% w/v sulfosalicylic acid. This resulted in the formation of a precipitate, and the reaction mixture was then refrigerated at 2–8 °C. After 1 hr, the samples were centrifuged at 4 °C and a rotation speed of 1200*g* for 15 min. The resulting pellets were discarded, leaving behind the supernatant. Next, 100 µl of the supernatant was mixed with 2.7 ml of 0.1 M phosphate buffer (pH 8) and 200 µl of 0.1 M DTNB. This mixture exhibited a pale yellow color. The color intensity was measured at a wavelength of 412 nm using a UV-visible spectrophotometer. To calculate the results, the chromophore molar extinction value of 1.36 $\times 10^4$ M^{-1} cm^{-1} was applied. The final results of the GSH assay were expressed as nM of GSH/min/mg of protein.

Estimation of superoxide dismutase (SOD) activity

The activity of SOD was determined following the method described by Kono, (1978). The assay utilized a solution containing 0.1 mM EDTA, 50 mM sodium carbonate, and 96 mM nitroblue tetrazolium. In this procedure, 2 ml of the aforementioned mixture was placed in a cuvette. To this, 50 µl of homogenate and 50 µl of hydroxylamine hydrochloride (pH 6.0) were added. The cuvette was then subjected to observation for 2 min, with measurements of the change in optical density taken at 560 nm at 30-second intervals using a UV-Vis spectrophotometer. The results obtained from the assay were expressed as SOD units/mg of protein.

Estimation of catalase (CAT) activity

Catalase activity was determined using the method described by Claiborne, (1985). The assay mixture comprised 1.95 ml of phosphate buffer (0.05 M, pH 7.0), 1.0 ml of hydrogen peroxide (0.019 M), and 50 µl of tissue homogenate (10%), resulting in a final volume of 3.0 ml. The changes in absorbance were measured at 240 nm using a UV-Vis

spectrophotometer. The results were expressed as µM of hydrogen peroxide decomposed/min/mg of protein.

Estimation of malonaldehyde (MDA) activity

The MDA is a substance that is generated as a result of lipid peroxidation (LPO), serving as an indicator of oxidative stress was estimated as per the protocol of Wills, (1966). For the LPO assay, 100 µl of tissue homogenate was mixed with 100 µl of 0.1 M Tris-HCl (pH 7.4). The mixture was then incubated in a temperature-controlled incubator at 37 °C for duration of 2 hrs. After the incubation period, the mixture was added with 200 µl of 10% TCA and subsequently subjected to centrifugation at 1000*g* for 10 min. Afterward, 200 µl of the resulting supernatant was collected and added to 200 µl of a 0.67% w/v TBA (thiobarbituric acid) solution. All the samples were then heated in boiling water for 10 min, resulting in the production of a pink color. After cooling, 200 µl of distilled water was added to each sample, and the absorbance was measured at 532 nm using a UV-visible spectrophotometer. The molar extinction coefficient using the results was calculated as 1.56×10^5 M^{-1} cm^{-1} and values were expressed as nM of MDA/min/mg of protein.

Estimation of nitrite activity

The nitric oxide molecule has a short lifespan and undergoes spontaneous oxidation to form nitrite and nitrate. The plasma levels of nitrite were determined following the method described by Green et al. (1982). To measure nitrite levels, equal volumes (100 µl) of tissue homogenate samples were combined with 100 µl of Griess reagent. The Griess reagent consisted of 1% sulphanilamide, 5% phosphoric acid and 0.1% naphthyl ethylenediamine dihydrochloride. This mixture was then incubated in a dark place at a temperature of 25–30 °C for 10 min. After incubation, absorbance readings were taken using a UV-visible

spectrophotometer at a wavelength of 540 nm. To determine the nitrite concentrations in the samples, a standard curve of sodium nitrite solution was used. The nitrite values were expressed as nM of nitrite/min/mg of protein.

Estimation of protein carbonylation (PCO) assay

The PCO activity was assessed using the method described by Ciaraldi et al. (1992). Briefly, 100 µl of tissue homogenate and 20 µl of dinitrophenylhydrazine (DNPH) were added to the sample mixture. The mixture was kept in a dark place and incubated for 60 min. The mixture was vortexed every 15 min. After the final vortex at 1 h, 120 µl of 20% TCA was added to the mixture. The mixture was subjected to incubation on ice for 15 min, followed by centrifugation at 10,000*g* for 5 min at 4 °C. After centrifugation, the resulting pellet was washed twice with 100 µl of TCA. Then, the ethanol mixture was washed with 100 µl of ethyl acetate: ethanol (1:1) mixture using centrifugation to wash the pellet. The resulting supernatant was discarded, and the pellet was allowed to dry for 5 min. The dried pellets were dispersed in 6 M guanidine. The mixture was incubated on a shaker at room temperature for 30 min. The absorbance of the compound was measured at 366 nm using a UV-visible spectrophotometer. Results were expressed as nM of PCO per mg of protein to determine the concentration of PCO.

Mitochondrial complex activity

Isolation of mitochondria

We followed the Berman et al., (1999) procedure for the mitochondrial complex. The dissected rat brain parts were homogenized in an ice-cold PBS solution containing EGTA (215 mM mannitol, 1 mM EGTA, 0.1% BSA, 20 mM HEPES, and 75 mM sucrose). The sample was centrifuged at 10,000*g* at 4 °C for 5 min. Following the second centrifugation,

the supernatants were transferred into the fresh tubes, placed in an isolation buffer containing EGTA, and centrifuged at 13,000*g* for 10 min at 4 °C. This process was repeated 3 times. It was first spun for 10 min with 1 mL of digitalize solution at 13000*g* at 4 °C for 10 min. The pellets from consecutive centrifuges were again suspended in an isolation buffer devoid of EGTA. This was applied to determine the mitochondrial complexes.

Mitochondrial complex I activity

The activity of nicotinamide adenine dinucleotide hydrogen (NADH) dehydrogenase (complex I) in mitochondria was assayed as described by King and Howard (1967). Briefly, a sample mixture contains 350 µl of 0.2 M glycylglycine buffer, 100 µl of 6 mM NADH, 200 µl of sodium, 2.4 ml of DDW, and 100 µl of 10.5 mM cytochrome-c. To this was added 10 µl of an isolated homogenate mitochondrial sample. The absorbance of the mixture was immediately measured using a UV-visible spectrophotometer. Absorption was assessed at each 60-second interval for a total of 3 min. The results were expressed as values of nM of NADH oxidation/min/mg of protein.

Mitochondrial complex II activity

The activity of succinate dehydrogenase (complex II) in mitochondria was assessed using the method described by King and Howard (1967). To prepare the reaction mixture, the following components were combined: 1.5 ml of 0.2 M sodium phosphate buffer (pH 7.8), 200 µl of 0.6 M potassium ferricyanide, 300 µl of succinic acid, 1% BSA (bovine serum albumin), 25 µl of 0.03 M potassium ferricyanide, and 1.75 ml of distilled deionized water (DDW). 25 µl of the mitochondrial sample was added to this reaction mixtureThe absorbance of the mixture was promptly measured at a wavelength of 420 nm using a UV-visible spectrophotometer. Measurements were taken at every 60-second interval for a total of 3 min.

394 The resulting calculated values were expressed as nM of substrate activity per min/mg of
395 protein.

396 **Mitochondrial Complex III activity**

397 The 3-(4,5-dimethylthiazol-2-yl)-2,5-diphenyl-H-tetrazolium bromide assay (complex
398 III) is also called the MTT assay (Mosmann et al., 1983). In a reaction tube, 100 µl of
399 mitochondrial homogenate was added to 10 µl of MTT. The mixture was incubated at 37 °C
400 for 3 hrs. During this incubation period, pale yellow MTT turns into formazan crystals. A
401 small amount of dimethyl sulfoxide (DMSO-50%) was added to dissolve the formazan
402 crystals. This allows the crystals to dissolve, resulting in a purple color. The absorbance of
403 the violet solution was immediately measured at a wavelength of 580 nm using an ELISA
404 reader.

405 **Mitochondrial complex IV activity**

406 The method described by Sotokasa et al. (1967) was used to estimate the activity of
407 cytochrome-c oxidase (complex IV) in mitochondria. The assay reaction mixture contained
408 100 µl of 0.3 mM reduced cytochrome-c (fixed with sodium borohydride crystals, pH 7.0 in
409 100 mM HCl) and 700 µl of 75 mM Contained PBS. 10 µl of mitochondrial sample was
410 added to the reaction mixture. The absorbance value of the mixture was immediately
411 measured at 550 nm using a spectrophotometer. Absorbance measurements were recorded at
412 60-second intervals for a total of 180 sec. Results were expressed as nM of cytochrome-c
413 oxidation/min/mg of protein.

414 **Molecular estimations**

415 The HS part, which is the primary location for learning and memory, was used to
416 calculate inflammatory cytokines including TNF-α (TNF-α ELIZA kit, Catalog #: RAB0479,

Sigma-Aldrich, US), IL-6 (Rat IL-6 ELISA Kit, Catalog #: RAB0311, Sigma-Aldrich, US), and C-reactive protein (CRP) (Rat C-Reactive Protein ELISA Kit (Catalog #: RAB0097, Sigma-Aldrich, US). According to the manufacturer's instructions, the levels of TNF-α, IL-6, and CRP in the hippocampal tissue homogenate were measured by an enzyme-linked immunosorbent assay (ELISA). TNF-α, IL-6, and CRP levels in the hippocampal were measured using standard curves for each. The results were expressed as pg/min/mg of protein and ng/mg of protein, respectively.

Protein estimation

Lowry's method was used for protein estimation by using bovine serum albumin as a standard (Lowry, 1951).

Histopathological analysis

Histopathological analysis was conducted after the completion of the behavioral experiments (Ahn et al., 2020; Mishra et al., 2018). Histopathological examination of vital organs was performed to determine whether degeneration occurred in the treated animals and whether there were any pathologic effects such as necrosis or inflammation in the experimental rats. According to this study, all experimental animals were euthanized using ketamine hydrochloride (80 mg/kg/b.w.) deep anesthesia. Then, vital organs such as the brain, heart, liver, kidney, and lung were collected and placed in 10% paraformaldehyde for 5 hrs. Also, vital organ parts were cut into 3 µm-thick sections using a paraffin wax cover and stained with hematoxylin and eosin for slide preparation. Prepared slides were magnified under a light microscope (AHBT-51, Olympus Vanox Research Microscope, Japan).

Molecular Docking (MD) Study

The structures of all ligands were obtained from the PubChem database in SDF (Structure-Data File) format (Luhrs, et al., 2005). The PubChem database, accessible at https://pubchem.ncbi.nlm.nih.gov, provided the necessary ligand information. Chem3D Pro 12.0 software was utilized to convert the SDF files to PDB (Protein Data Bank) format. This conversion allowed for compatibility with the subsequent steps of the docking study. Auto Dock Tools 1.5.7 was employed to prepare the ligands for docking. Polar and nonpolar hydrogen molecules were added to the ligands, aiding in the subsequent docking process (Jokara et al., 2020). Ligands prepared using the GAUSSIAN03 package underwent optimization. The DFT (Density Functional Theory) method, employing the 6-311G** basis set was used for the optimization process. The 3D structure of Aβ fibrils $_{(1–42)}$, identified as 2BEG, was retrieved from the Protein Data Bank (PDB). The PDB, a comprehensive repository of protein structures, provided the required structure for the docking study. AutoDockTools 1.5.7 software facilitated the docking process. Ligands were docked with the Aβ fibrils (1–42) structure, enabling the analysis of potential interactions. Pymol and DISCOVERY STUDIO VISUALIZER (26) software was utilized for the analysis of docking interactions. These tools allowed for the examination and visualization of the molecular interactions resulting from the docking study.

Statistical analysis

The characterization study was quantified using Origin Pro software (Origin Pro-2019 b). The Graph Pad Prism software (Graph Pad Prism 9, San Diego, CA, USA) was used for all the statistical analysis. Behavioral assessment was evaluated by a two-way analysis of variance (ANOVA) followed by Bonferroni’s post hoc for multiple comparisons. The biochemical data was analyzed using a one-way analysis of variance (ANOVA), followed by Tukey's test for conducting multiple comparisons. The results were expressed as the mean ±

standard deviation (mean ± SD). All the results of the probability tests were measured to be significantly different at $p < 0.05$.

Results

Characterization studies

UV-Vis spectrophotometer

The synthesis of the CH/PLA/MgONCs was confirmed by using UV–vis spectroscopy. The spectral analysis was conducted in the spectral range of 200–500 nm, as shown in Fig. (1A) and the absorbance value of 282 nm were confirmed.

FT-IR results

The FT-IR spectral range of the CH/PLA/MgONCs is shown in Fig. 1B. A broad range of 3200–3800 cm^{-1} shows the stretching vibrations of the O-H and N-H groups. The stretching vibration peaks of amide I (C=O) at 1521 cm^{-1} and amide III (N=H) at 1390 cm^{-1} show a significant peak of chitosan presence, as shown in Fig. 1B. The stretching vibrations of MgO are confirmed by magnesium peaks (Mg-O) in the wavenumber region of 451 to 515 cm^{-1}. The band spectral range of 1957 to 2238 cm^{-1} for C=O stretching vibrations is stronger in PLA. The stretching of the COO^- the group was given absorption values between the ranges of 1058 cm^{-1}. The significant peak at 1385 cm^{-1} is due to the combined frequency of CH-OH groups.

Swelling properties of CH/PLA/MgONCs

The swelling properties of CH/PLA/MgONCs were measured from 5 min to 24 h (Fig. 1C). It was found that the swelling ratios of CH, PLA, MgO, and CH/PLA/MgONCs gradually increased. Swelling and weight ratios showed the most increased results (96.23 ±

3.28%) in CH/PLA/MgONCs. Furthermore, at 20 and 24 h higher weight limits, CH/PLA/MgONCs were completely degraded. As a result, CH/PLA/MgONCs were used for further research.

In vitro drug release of CH/PLA/MgONCs

The cumulative drug release percentages (CDR) of CH, PLA, MgO, and CH/PLA/MgONCs are shown in Fig. 1D. The release rate of the compounds CH, PLA, and MgO from CH/PLA/MgONCs was low, so the final release rate was also low. However, if it comes to MgO from CH/PLA/MgONCs, the MgO release was faster, and the final release rate was approximately 92.67 ± 2.28% to 97.52 ± 2.85%. The release rate of MgO was highly improved compared to other compounds of the hydrogel (Fig. 1D). Furthermore, the swelling analysis results were consistent with improved and possible release behavior of MgO from CH/PLA/MgONCs.

SEM-EDAX

The CH/PLA/MgONCs surface morphology analysis results are shown in Fig. 2. The prepared CH/PLA/MgONCs have a cauliflower-like spherical shape structure (Fig. 2A). EDAX spectrum analysis results confirm the presence of Mg (Fig. 2B). Also, EDAX mapping results confirm the presence of O, Mg, Si, and Cl (Fig. 2C).

Behavioral assessments

Effect on MWM test

Spatial memory function was evaluated by using the MWM test, results are shown in Fig. 3. There was no significant change on day 1 of the trial phase for all experimental groups. On days 2, 3, 4, and 5, the ICV-STZ-treated group exhibited a significantly longer (p

507 < 0.001) escape latency compared with control group. The treated group with CH, MgO,
508 CH/MgO, and escape latency of CH/PLA/MgONCs showed significantly attenuated ($F_{(5,15)}$ =
509 19.70, $p < 0.0001$) when compared with ICV-STZ-treated group (Fig. 3B). The time spent in
510 the target quadrant (TSTQ) and platform crossing time was significantly attenuated ($p <$
511 0.001) in the ICV-STZ group compared with control group. Significant improvement in the
512 TSTQ ($F_{(5,30)}$ = 122.5, $p < 0.0001$) and platform crossing time ($F_{(5,30)}$ = 87.16, $p < 0.0001$)
513 was observed with CH, MgO, CH/MgO, and CH/PLA/MgONCs as compared with ICV-STZ-
514 treated group (Fig. 3C, D). Moreover, the error time in the ICV-STZ-treated group showed a
515 significant improvement ($p < 0.001$) compared with control group. The treated group with
516 CH, MgO, CH/MgO, and CH/PLA/MgONCs resulted in a significant decrease ($F_{(5,30)}$ =
517 112.8, $p < 0.0001$) in error time compared with ICV-STZ-treated group (Fig. 3E).

518 **Effect on PA test**

519 The ICV-STZ-treated group exhibited a significant reduction ($p < 0.001$) in STL
520 compared with control group. The treatment with CH, MgO, CH/MgO, and
521 CH/PLA/MgONCs resulted in a significant improvement ($F_{(5,15)}$ = 68.45, $p < 0.0001$) of STL
522 when compared with ICV-STZ-treated group (Fig. 4A). Notably, the group treated with
523 CH/PLA/MgONCs showed even greater improvement in STL compared with ICV-STZ
524 treated group, as shown in Fig. 4A.

525 **Effect on Y-maze test**

526 The ICV-STZ-treated group demonstrated a significant improvement ($p < 0.0001$) in
527 the overall number of arm entries compared with control group. The treatment with CH,
528 MgO, CH/MgO, and CH/PLA/MgONCs resulted in a significant attenuation ($F_{(5,15)}$ = 53.99,
529 $p < 0.0001$) of the number of arm entries when compared with ICV-STZ-treated group.

Specifically, the CH/PLA/MgONCs experimental group exhibited a significant decrease ($p < 0.0001$) in the number of arm entries compared with ICV-STZ-treated group, as depicted in Fig. 4B.

Biochemical measurement

Effect on AChE activity

The rats that received ICV-STZ-treated group exhibited a significant improvement of AChE activity in the CS ($p < 0.01$) and HS ($p < 0.0001$) regions when compared with control group (Fig. 5A). However, treatment with CH, MgO, CH/MgO, and CH/PLA/MgONCs resulted in a significant attenuation of CS ($F_{(5,30)} = 94.41$, $p < 0.0001$) and HS ($F_{(5,30)} = 119.9$, $p < 0.0001$) AChE activity when compared with ICV-STZ-treated group. Notably, the CH/PLA/MgONCs at a dose of 10 mg/kg showed higher control over AChE activity in CS and HS when compared with ICV-STZ group.

Effect on SOD activity

The SOD levels in animals treated with ICV-STZ-treated group were found to be significantly attenuated in the CS ($p < 0.01$) and HS ($p < 0.0001$) compared with control group (Fig. 5B). However, the group treated with CH, MgO, CH/MgO, and CH/PLA/MgONCs showed a significant improvement in SOD levels in the CS ($F_{(5,30)} = 83.53$, $p < 0.0001$) and HS ($F_{(5,30)} = 87.69$, $p < 0.0001$) when compared with the ICV-STZ-treated group. Furthermore, the treatment with CH/PLA/MgONCs showed a higher improvement in the SOD levels of CS and HS brain regions.

Effect on CAT activity

The ICV-STZ treatment led to a significant reduction in CAT activity in both the CS ($p < 0.0001$) and HS ($p < 0.0001$) when compared with control animals (Fig. 5C). However,

553 treatment with CH, MgO, CH/MgONCs, and CH/PLA/MgONCs significantly improved CAT
554 activity in the CS ($F_{(5,30)}$ = 130.3, $p < 0.0001$) and HS ($F_{(5,30)}$ = 145.4, $p < 0.0001$) compared
555 with ICV-STZ-treated group. Notably, treatment with the CH/PLA/MgONCs group
556 effectively restored CAT activity in the CS and HS indicating an enhanced endogenous
557 antioxidant defense mechanism.

558 **Effect on GSH activity**

559 The animals treated with ICV-STZ exhibited a significant decrease in both CS ($p <$
560 0.01) and HS ($p < 0.0001$) in GSH levels compared with the control group. However,
561 treatment with CH, MgO, CH/MgONCs, and CH/PLA/MgONCs demonstrated a significant
562 restoration of GSH levels in the CS ($F_{(5,30)}$ = 99.45, $p < 0.0001$) and HS ($F_{(5,30)}$ = 121.2, $p <$
563 0.0001), indicating their potent antioxidant potential. Furthermore, treatment with
564 CH/PLA/MgONCs showed a higher improvement in GSH levels in the CS ($p < 0.001$) and
565 HS ($p < 0.05$) compared with ICV-STZ-treated animals (Fig. 5D).

566 **Effect on MDA activity**

567 The extent of lipid per oxidative damage caused by oxidative stress can be measured
568 by elevated levels of malondialdehyde (MDA) in brain tissue. In the ICV-STZ-treated
569 animals, there was a significantly increased MDA level observed in both the CS ($p < 0.0001$)
570 and the HS ($p < 0.01$) when compared with control animals (Table 1). However, treatment
571 with CH, MgO, CH/MgONCs, and CH/PLA/MgONCs significantly attenuated the MDA
572 levels in the CS ($F_{(5,30)}$ = 48.01, $p < 0.0001$) and HS ($F_{(5,30)}$ = 60.46, $p < 0.0001$) compared
573 with ICV-STZ-treated animals. Notably, treatment with CH/PLA/MgONCs effectively
574 controlled MDA levels in both the CS and HS when compared with ICV-STZ-treated
575 animals, indicating an improvement in oxidative stress.

576 **Effect on nitrite activity**

577 Nitric oxide (NO) is a molecule that has a short lifespan, and its release is increased in
578 the injured brain, leading to nitrative stress. In the present study, it was observed that the
579 plasma nitrite levels in the CS ($F_{(5,30)}$ = 140.1, $p < 0.0001$) and HS ($F_{(5,30)}$ = 159.2, $p <$
580 0.0001) were significantly improved in ICV-STZ-treated animals compared with control
581 animals. However, the administration of CH, MgO, CH/MgO, and CH/PLA/MgONCs
582 resulted in a significant reduction in the CS ($p < 0.001$) and HS ($p < 0.0001$) when compared
583 with ICV-STZ animals, indicating a reduction in nitrative stress. Notably, the treatment with
584 the CH/PLA/MgONCs group significantly controlled the plasma nitrite levels in both the CS
585 ($p < 0.0001$) and HS ($p < 0.0001$) when compared with ICV-STZ-treated animals, further
586 indicating a reduction in nitrative stress (Table 1).

587 **Effect on PCO activity**

588 The animals treated with the ICV-STZ-treated group showed a significant increase in
589 the activity of PCO in both the CS ($p < 0.01$) and HS ($p < 0.0001$) compared with control
590 animals (Table 1). However, treatment with CH, MgO, CH/MgONCs, and
591 CH/PLA/MgONCs significantly attenuated the PCO activity in the CS ($F_{(5,30)}$ = 75.87, $p <$
592 0.0001) and HS ($F_{(5,30)}$ = 81.73, $p < 0.0001$) compared with animals treated with ICV-STZ.
593 Additionally, the group treated with CH/PLA/MgONCs showed a higher level of decrease in
594 PCO activity in the CS and HS when compared with animals treated with ICV-STZ.

595 **Mitochondrial complex (I, II, III, and IV) activity**

596 The ICV-STZ-treated group exhibited a significant attenuation in the levels of all
597 mitochondrial complex activities (I, II, III, and IV) in the CS ($p < 0.0001$) and HS ($p <$
598 0.0001) regions when compared with control rats, as presented in Table 2.

599 In comparison to the ICV-STZ-treated rats, the administration of CH, MgO,
600 CH/MgONCs, and CH/PLA/MgONCs treatments in the experimental groups resulted in

significantly increased activities in the mitochondrial complex I activity of the CS ($F_{(5,30)}$ = 131.2, $p < 0.0001$) and HS ($F_{(5,30)}$ = 143.8, $p < 0.0001$), mitochondrial complex II activity of the CS ($F_{(5,30)}$ = 139.1, $p < 0.0001$) and HS ($F_{(5,30)}$ = 148.6, $p < 0.0001$), mitochondrial complex III activity of the CS ($F_{(5,30)}$ = 127.4, $p < 0.0001$) and HS ($F_{(5,30)}$ = 140.4, $p < 0.0001$), and mitochondrial complex IV activity of the CS ($F_{(5,30)}$ = 153.1, $p < 0.0001$) and HS ($F_{(5,30)}$ = 169.7, $p < 0.0001$). Interestingly, the treatment group receiving CH/PLA/MgONCs demonstrated highly improved activities in all mitochondrial complex compared with ICV-STZ-treated groups (Table 2).

Molecular estimation

TNF-α, IL-6, and CRP were evaluated in the HS, and The results demonstrated a significant improvement ($p < 0.0001$) in the levels of the aforementioned three markers in the ICV-STZ-treated group compared with the control group. However, TNF-α level was decreased significantly HS ($F_{(5,30)}$ = 143.8, $p < 0.0001$) with the treatment with CH, MgO, CH/MgONCs, and CH/PLA/MgONCs as compared to ICV-STZ-treated group (Fig. 6A). The treatment with CH, MgO, CH/MgONCs, and CH/PLA/MgONCs significantly decreased HS ($F_{(5,30)}$ = 90.26, $p < 0.0001$) the IL-6 level when compared to ICV-STZ-treated group (Fig. 6B). The treatment with CH, MgO, CH/MgONCs, and CH/PLA/MgONCs significantly decreased HS ($F_{(5,30)}$ = 106.1, $p < 0.0001$) the CRP level when compared with ICV-STZ-treated group (Fig. 6C). Interestingly, all the treated groups with CH/PLA/MgONCs had highly controlled TNF-α, IL-6, and CRP levels when compared to ICV-STZ-treated group.

Histopathological analysis

As shown in Fig. 7, the histopathological results are shown in the CS and HS regions of the brain. In this study, results showed that the control group had healthy neurons with oval shapes and clear cytoplasm. But, in contrast, brain regions CS and HS of ICV-STZ-

treated rats showed a higher number of damaged neurons, distorted patterning, and nuclear damage compared to control rats. However, treatment of different experimental groups with CH/PLA/MgONCs effectively restored the lost neuronal damage compared to ICV-STZ-treated rats and showed oval-shaped, healthy embryos and a high number of healthy neurons with clear cytoplasm (Fig 7). Also, H and E histopathological results of major organs in experimental rats such as the heart, lung, liver, and kidney are described in Fig. 8. In this study, ICV-STZ-treated rats showed minor tissue and cell changes compared with control group. However, different experimental groups indicated that CH/PLA/MgONCs treatment contained more advanced tissues and more malignant cells in major organs such as the heart, liver, lung, and kidney. Furthermore, the results of this study confirm that treatment with CH/PLA/MgONCs has healthier cells and tissues compared with ICV-STZ in all major organs (Fig. 8).

Molecular docking

The nature of the best binding for key phytochemicals against Aβ protein was analyzed using an MD study. Docking scores were obtained from MD results, in which (A) caffeic acid, (B) dihydrobenzoic acid, (C) ferulic acid, and (D) epirosmanol have binding scores of -6.74, -3.75, -4.56, and -5.93, respectively. Docking values for 3D and 2D interpolated structures were obtained using Discovery Studio for Complex. This study describes that caffeic acid and epirosmanol phytochemicals have stable and high binding affinity against the Aβ protein (Fig. 9).

Discussion

Biomaterial-based nano-drug delivery systems possess important properties such as good drug release, physicochemical properties, biocompatibility, biodegradability,

environmental reactivity, and pharmacological activity (Joseph et al., 2022; Sahu et al., 2021). At the same time, hydrogel-based nanocomposite biomaterials are a good supporting platform for particulate drug delivery systems based on their pore size, various functional groups, and properties (Zarrintaj et al., 2020). Biomaterial-based nanocomposite improves drug stability and has the advantage of sustained-release products, showing a wide range of advances and application features (Zhuang et al., 2021). In this study, CO and OH functional groups in CH, PLA, and MgO demonstrate strong electrostatic interactions, which are confirmed. Also, most of the concentrated CH and PLA characteristic peaks show a strong bond between the biomaterial-based hydrogels. The spectral results of CH/PLA/MgONCs demonstrate that they have excellent functional groups and synergistic drug-release properties. The results of SEM analysis confirmed that the CH/PLA/MgONCs were cauliflower-like and spherical. Several studies have shown that spherical shapes are more suitable for drug delivery applications and have a higher chance of cell passage. This study describes the effect of CH/PLA/MgONCs treatment on oxidative stress, neuronal damage, mitochondrial changes, and cholinergic activity in ICV-STZ-induced AD.

Administration of ICV-STZ injection induces brain insulin resistance and mimics pathological and behavioral changes observed in sporadic AD, including cognitive dysfunction, neurotoxicity and mitochondrial dysfunction (Akhtar et al., 2021). Even at sub-diabetogenic doses, ICV-STZ induces oxidative stress, the release of inflammatory cytokines, mitochondrial dysfunction, impaired insulin signaling, and memory impairment (Yamini, et al., 2018). As a result, the CS and HS regions of the brain experience impairments in insulin signaling, leading to a neurodegenerative process and subsequent cognitive dysfunction. Therefore, several studies indicate that the ICV-STZ model serves as a trusted model of AD. However, ICV-STZ administration, mainly in animal models, has received much attention in

AD models such as neurological and behavioral disorders (Moghaddam et al., 2018; Mishra et al., 2023).

In the MWM test, the ICV administration of STZ resulted in significant impairments in learning and memory performance. This was evident through a higher number of errors and an increased duration of time required reaching the target platform during the training phase, indicating memory dysfunctions (Zhou et al., 2019). Additionally, the ICV-STZ rats displayed a progressive increase in mean escape latency and swim path length during training trials, along with a decreased number of errors (Akhtar et al., 2021). These findings further support the presence of impaired retention memory in ICV-STZ rats during the spatial navigation task in the MWM test. The animals treated with CH/PLA/MgONCs exhibited a high decrease in mean escape latency and were able to find the hidden platform faster. Consistent with previous findings, our results indicate that treatment with vitamin D3 improved spatial learning and memory functions in the MWM test (Yamini et al., 2018).

The PA test is used to measure non-spatial memory and attention (Taheri et al., 2023). Also, a higher improvement in positive avoidance tests was observed after CH/PLA/MgONCs treatment. Additionally, CH/PLA/MgONCs treatment led to a higher reduction in transfer latency into the enclosed arm, indicating improved retention memory compared to both ICV-STZ animals and the CH/PLA/MgONCs treatment group in the Y maze test. Furthermore, CH/PLA/MgONCs treatment strategies improved non-spatial learning and memory functions and the CH/PLA/MgONCs treatment demonstrated superior efficacy in mitigating ICV-STZ-induced neuronal damage and behavioral dysfunction.

The STZ overproduces and worsens the activity of AChE in the brain, leading to cholinergic dysfunction. Furthermore, it is well established that increased cholinergic activity is associated with improved cerebral blood flow (Zhou et al., 2019). The enzyme AChE

breaks down acetylcholine, a neurotransmitter that plays a role in cognition and memory through the modulation of synaptic transmission (Varesi et al., 2023). Therefore, AChE inhibition is a prime and promising target for AD. In the present study, results illustrate that CH/PLA/MgONCs treatment significantly targets and suppresses AChE overproduction. This shows that a lower AChE level significantly restores the loss of cholinergic neurons.

The brain is very metabolically active and lacks adequate internal defense mechanisms, making it highly susceptible to oxidative damage caused by free radicals (Bhatti et al., 2022). Oxidative stress in the brain can be effectively countered by endogenous antioxidant enzymes such as GSH, SOD, CAT, and GPx and oxidation plays a critical role in the development and progression of neurodegenerative disorders such as AD (Ali et al., 2020). Increased neuronal oxidative stress in ICV-STZ-treated rats was observed with damage to essential cellular components such as lipids, proteins, DNA, and RNA. This contributes to impaired hippocampal synaptic plasticity and neurogenesis (Tramutola et al., 2017). In this study, treatment with CH/PLA/MgONCs highly reduced the oxidative stress induced by ICV-STZ and restored the endogenous antioxidant defense system to normal levels. These findings are consistent with previous research demonstrating restoration of reduced endogenous antioxidant defense systems and highlighting the antioxidant activity of CH/PLA/MgONCs in justifying oxidative damage (Yin et al., 2022; Ali et al., 2020).

In the current study, the administration of ICV-STZ resulted in an exacerbation of neuronal oxidative stress, leading to peroxidative damage of membrane lipids and an increase in the generation of MDA (Verma et al., 2020). This, in turn, intensified neuronal damage, affecting critical cellular biomolecules. MDA is commonly used as a biomarker to measure the extent of oxidative damage. The results emphasize the substantial role of oxidative and nitrosative stress in the progression of AD. Specifically, in this study, ICV-STZ

administration further heightened the levels of MDA and nitrite in the HS and CS regions of the rat brain (Gaur et al., 2021; Mishra et al., 2023). In our study, treatment with CH/PLA/MgONCs demonstrated an effective reduction of oxidative damage caused by the overproduction of free radicals in the CS and HS regions, as indicated by decreased levels of MDA. Additionally, CH/PLA/MgONCs treatment highly decreased plasma total nitric oxide levels. These findings indicate that CH/PLA/MgONCs treatment not only reduced oxidative-nitrative damage but also protected against neuronal damage. These results are consistent with previous experimental evidence that targeting can reduce oxidative damage (Yamini et al., 2022).

Mitochondria are responsible for the majority of endogenous ROS generation in reacted with oxidative stress (Mishra et al., 2023). The subsequent peroxidation of mitochondrial components leads to dysfunction in the electron transport chain. This interplay between mitochondrial dysfunction and oxidative stress plays a crucial role in initiating ROS production, which in turn contributes to the development of AD. Neuronal mitochondrial dysfunction can either be a result of or a cause of the generation of ROS, making it a key characteristic in the ICV-STZ-induced rats (Akhtar et al., 2021). In this study, we observed a higher decrease in the activity of mitochondrial complexes I, II, III, and IV in both the CS and HS regions following ICV-STZ administration. However, treatment with CH/PLA/MgONCs resulted in a high restoration of mitochondrial complex activity in various treatment groups. Notably, the activity of all mitochondrial complexes (I, II, III, and IV) in the CH/PLA/MgONCs-treated groups showed greater improvement compared with ICV-STZ-treated group. This improvement in mitochondrial complex activity was accompanied by a significant reduction in oxidative stress, suggesting enhanced energy production in the brain (Yamini et al., 2022).

Neuroinflammation is a key feature of synaptic dysfunction and neurodegeneration in the ICV-STZ model of AD (Xiang et al., 2022). STZ activates microglia to release pro-inflammatory cytokines such as TNF-α and IL-6, leading to neuroinflammation. Neuroinflammation is driven by activated glial cells, particularly microglia and astrocytes, and peripheral leukocytes, which release proinflammatory cytokines such as TNF-a, and IL-6 in large quantities in response to various neurological disease processes (Mishra et al., 2018; Verma et al., 2020). Therefore, targeting anti-inflammatory mechanisms may be beneficial in the treatment of AD. Some research suggests that increased levels of TNF-α, IL-6, and CRP, which are produced as a result of ICV-STZ administration, are associated with neurodegenerative diseases such as AD (Yamini et al., 2018). In the present study, ICV-STZ-induced overproduction of TNF-α, IL-6, and CRP levels were effectively attenuated in the CS and HS of the CH/PLA/MgONCs-treated group, which may be well correlated with the reversal of neuronal injury. These results support the idea that neuronal survival can be restored through the transcription of proinflammatory cytokines and transcription factors. This reduction in inflammation may be correlated with the reversal of neuronal damage, indicating improved cell survival. These findings support the notion that the transcription of chemokines, proinflammatory cytokines, and transcription factors can contribute to the restoration of neuronal survival. The results of this study align with previous evidence highlighting the anti-inflammatory properties of the treatment (Akhtar et al., 2020).

Histological analysis provides a means to evaluate neuronal damage and the effects of drugs. The hippocampal is widely acknowledged for its vital role in learning and memory processes. Both CS and HS neurons are known to contribute to the modulation of AD pathology, which frequently involves substantial neuronal damage within these brain regions (Ahn et al., 2020). Previous studies conducted by our team have revealed that the administration of ICV-STZ can induce neurodegeneration specifically in the HS.

Histopathological evidence further suggests that ICV-STZ promotes structural and functional impairments in both the CS and HS neuronal structures, accompanied by the presence of β-amyloid peptide-like aggregates within brain capillaries (Mishra et al., 2018). In our current study, we observed notable changes in morphology, neuronal damage, and neuronal loss in the CS and hippocampal regions (CA1, CA3, and DG) of animals with AD induced by ICV-STZ. However, upon treatment with CH/PLA/MgONCs, we observed the presence of numerous healthy neurons with clear cytoplasm as well as the emergence of new oval-shaped neurons in the CS and hippocampal regions (CA1, CA3, and DG). This indicates the potential neurotherapeutic benefits of CH/PLA/MgONCs and aligns with the neurobiological and biochemical findings. Furthermore, these results are consistent with the outcomes of behavioral tests and biochemical assays. Therefore, our study results suggest that CH/PLA/MgONCs may serve as an effective agent for reducing neurotoxicity by counteracting the oxidative damage induced by ICV-STZ. Furthermore, in the experimental group of rats with internal organs, histopathological examination revealed that ICV-STZ induced relatively minor tissue and cellular structural damage. However, in the treatment groups receiving CH/PLA/MgONCs, there was a more pronounced improvement in tissue quality, with the presence of clear and healthy cells observed in major organs such as the heart, lung, kidney, and liver. These morphological characteristics serve as evidence of the functional benefits and enhanced functioning of these important organs. Importantly, the results strongly suggest that CH/PLA/MgONCs offer a promising approach to promoting tissue and cellular regeneration non-toxic and without any associated side effects (Rajkumar et al., 2022b).

Intermolecular interaction analysis results from the *in silico* study show that the ligands are stable and have a high binding capacity (Pasieka et al., 2021). In the major phytochemicals such as caffeic acid, dihydro benzoic acid, ferulic acid, and epirosmanol

794 binding with the Aβ protein complex, the residue creates hydrogen bonding interactions
795 parallel to the molecular docking complex, and the remaining enzyme interactions confirm
796 that the complex is neutralized during the MD. In phytochemical binding capacity, new
797 interactions with different residues are observed as a result of docking analysis.
798 Phytochemicals active site has been proven to perform best in MD study (Jokara et al., 2020;
799 Pasieka et al., 2021).

800 Conclusion

801 In conclusion, the characterization results of CH/PLA/MgONCs, FT-IR with various
802 functional groups, and SEM results showed that they have cauliflower-like spherical shapes.
803 Physical property studies confirmed the high swelling properties and experimental drug
804 release permeability of CH/PLA/MgONCs. In ICV-STZ-treated rats, neurotoxicity,
805 mitochondrial dysfunction, oxidative stress, and neuronal damage were observed. The
806 behavioral tests conducted in this study revealed that treatment with CH/PLA/MgONCs
807 effectively improved spatial and non-spatial memory functions in experimental rats.
808 Furthermore, CH/PLA/MgONCs treatment significantly reduced the overproduction of
809 AChE, MDA, and nitric oxide in the CS and HS regions while enhancing the activities of
810 antioxidant enzymes such as GSH, SOD, and CAT. Additionally, CH/PLA/MgONCs
811 treatment improved mitochondrial complex functions in the CS and HS while decreasing
812 molecular cytokines. Histopathological analysis showed that the groups treated with
813 CH/PLA/MgONCs displayed healthy neurons with clear cytoplasm. Molecular docking
814 studies indicated that major phytochemicals exhibited stable and significant binding affinities
815 to Aβ protein. In conclusion, this study demonstrates that CH/PLA/MgONCs treatment
816 effectively alleviates AD and highlights its significance as a new and improved therapeutic
817 approach for AD treatment.

Author contributions: All authors performed the literature research, analyzed, and critically discussed the data. The authors also contributed to elaborating the figures and approving the final version of the manuscript.

Funding: This work was financially supported and received from the University Research Fellow (URF) from Periyar University, Salem-636 011, Tamil Nadu, India (PU/AD-3/URF/013805/2019).

Ethics approval: The Committee for the Purpose of Control and Supervision of Experiments on Animals (CPCSEA), Government of India, approved all treatment and experimental procedures of the current study. All research and animal care procedures were in accordance with the Institutional Animal Ethical Committee (PU/IAEC/2020/M1/19) of Periyar University, Tamil Nadu, India.

Consent to participate: Not applicable.

Data availability: Available upon request.

Code availability: Not applicable

Consent for publication: All author agree for publication

Conflict of interest: There are no conflicts of interest to declare.

Declarations:

Declaration of Competing Interest: The authors report that they have no declarations of interest.

Reference

838 Ahn Y, Seo J, Park J, Won J, Yeo HG, Kim K, Jeon CY, Huh JW, Lee SR, Lee DS, Lee Y
839 (2020) Synaptic loss and amyloid-beta alterations in the rodent hippocampus induced
840 by streptozotocin injection into the cisterna magna. Lab Anim Res 36, 1-6

841 Akhtar A, Dhaliwal J, Sah SP (2021) 7, 8-Dihydroxyflavone improves cognitive functions in
842 ICV-STZ rat model of sporadic Alzheimer's disease by reversing oxidative stress,
843 mitochondrial dysfunction, and insulin resistance. Psychopharmaco 238, 1991-2009

844 Alhodieb FS, Barkat MA, Barkat HA, Ab Hadi H, Khan MI, Ashfaq F, Rahman MA, Hassan,
845 M.Z, Alanezi AA (2022) Chitosan-modified nanocarriers as carriers for anticancer
846 drug delivery: Promises and hurdles. Int J Biol macromol 217, 457-469

847 Ali SS, Ahsan H, Zia MK, Siddiqui T, Khan FH (2020) Understanding oxidants and
848 antioxidants: Classical team with new players. J Food Biochem 44(3), 13145

849 Arduino I, Depalo N, Re F, Dal Magro R, Panniello A, Margiotta N, Fanizza E, Lopalco, A,
850 Laquintana V, Cutrignelli A, Lopedota AA (2020) PEGylated solid lipid nanoparticles
851 for brain delivery of lipophilic kite-platin Pt (IV) prodrugs: An *in vitro* study. Int J
852 Pharm 583, 119351

853 Berman SB, Hastings TG (1999) Dopamine oxidation alters mitochondrial respiration and
854 induces permeability transition in brain mitochondria: implications for Parkinson's
855 disease. J Neurochem 73(3), 1127-1137

856 Bhatti JS, Sehrawat A, Mishra J, Sidhu IS, Navik U, Khullar N, Kumar S, Bhatti GK, Reddy
857 PH (2022) Oxidative stress in the pathophysiology of type 2 diabetes and related
858 complications: Current therapeutics strategies and future perspectives. Free Radic Biol
859 Med 184, 114-134

860 Ciaraldi TP, el-Roeiy ALBERT, Madar ZECHARIA, Reichart DONNA, Olefsky JM, Yen,
861 SS (1992) Cellular mechanisms of insulin resistance in polycystic ovarian syndrome. J.
862 Clin Endocrinol Metab 75(2), 577-583

863 Claiborne AJFCP (1985) Handbook of methods for oxygen radical research. Florida: CRC
864 Press Boca Raton 283-4

865 Conrad CD, Galea LA, Kuroda Y, McEwen BS, (1996) Chronic stress impairs rat spatial
866 memory on the Y maze, and this effect is blocked by tianeptine treatment. Behav
867 Neurosci 110(6), 1321

868 Da Matta FM, do Amaral JA, Rena AB (1999) Growth periodicity in trees of Coffea arabica
869 L. in relation to nitrogen supply and nitrate reductase activity. Field Crops Res 60(3),
870 223-229

871 Dhand V, Soumya L, Bharadwaj S, Chakra S, Bhatt D, Sreedhar B (2016) Green synthesis of
872 silver nanoparticles using Coffea arabica seed extract and its antibacterial activity.
873 Mater Sci Eng C 58, 36-43

874 Di Lorenzo A, Curti V, C Tenore G, M Nabavi S, Daglia M (2017) Effects of tea and coffee
875 consumption on cardiovascular diseases and relative risk factors: an update. Curr
876 Pharm Des 23(17), 2474-2487

877 Duangjai A, Suphrom N, Wungrath J, Ontawong A, Nuengchamnong N, Yosboonruang A
878 (2016) Comparison of antioxidant, antimicrobial activities and chemical profiles of
879 three coffee (Coffea arabica L.) pulp aqueous extracts. Integr Med Res 5(4), 324-331

880 Ellman GL, Courtney KD, Andres Jr, V, Featherstone RM, (1961) A new and rapid
881 colorimetric determination of acetylcholinesterase activity. Biochem Pharmacol
882 7(2):88-95

883 Fernandes MDRV, Pfenning LH, Costa-Neto CMD, Heinrich TA, Alencar SMD, Lima
884 MAD, Ikegaki M, (2009) Biological activities of the fermentation extract of the
885 endophytic fungus Alternaria alternata isolated from *Coffea arabica* L. Braz J Pharm
886 Sci 45, 677-685

887 Gaur P, Prasad S, Kumar B, Sharma SK, Vats P, (2021) High-altitude hypoxia induced
888 reactive oxygen species generation, signaling, and mitigation approaches. Int J
889 Biometeorol 65, 601-615

890 Gong L, Zhang X, Ge K, Yin Y, Machuki JOA, Yang Y, Shi H, Geng D, Gao F (2021)
891 Carbon nitride-based nanocaptor: An intelligent nanosystem with metal ions chelating
892 effect for enhanced magnetic targeting phototherapy of Alzheimer's disease. Biomat
893 267, 120483

894 Green LC, Wagner DA, Glogowski J, Skipper PL, Wishnok JS, Tannenbaum SR (1982)
895 Analysis of nitrate, nitrite, and [15N] nitrate in biological fluids. Anal Biochem 126(1),
896 131-138

897 Islam MM, Shahruzzaman M, Biswas S, Sakib MN, Rashid TU (2020) Chitosan based
898 bioactive materials in tissue engineering applications-A review. Bioact Mater 5(1), 164-
899 183

900 Jollow DJ, Mitchell JR, Zampaglione NA, Gillette JR (1974) Bromobenzene-induced liver
901 necrosis. Protective role of glutathione and evidence for 3, 4-bromobenzene oxide as
902 the hepatotoxic metabolite. Pharmacol 11(3), 151-169

903 Joseph X, Akhil V, Arathi A, Mohanan PV (2022) Nanobiomaterials in support of drug
904 delivery related issues. Mater Sci Eng B 279, 115680

905 Kiattisin K, Nantarat T, Leelapornpisid P (2016) Evaluation of antioxidant and anti-
906 tyrosinase activities as well as stability of green and roasted coffee bean extracts from
907 Coffea arabica and Coffea canephora grown in Thailand. J Pharmacognosy Phytother 8
908 (10), 182-192

909 King TE, Howard RL (1967) Preparations and properties of soluble NADH dehydrogenases
910 from cardiac muscle. In Methods in enzymology. Academic Press (Vol. 10, 275-294)

911 Kono Y, (1978) Generation of superoxide radical during autoxidation of hydroxylamine and
912 an assay for superoxide dismutase. Arch Biochem Biophys 186 (1), 189-195

913 Liu D, Dai X, Ye L, Wang H, Qian H, Cheng H, Wang X (2023) Nanotechnology meets
914 glioblastoma multiforme: Emerging therapeutic strategies. Wiley Interdiscip Rev
915 Nanomed Nanobiotechnol 15(1), 1838

916 Lowry OH, Rosebrough NJ, Farr AL, Randall RJ, (1951) Protein measurement with the Folin
917 phenol reagent. J Biol Chem 193, 265-275

918 Luhrs T, Ritter C, Adrian M, Riek-Loher D, Bohrmann B, Dobeli H, Schubert D (2005) Riek
919 R, 3D structure of Alzheimer's amyloid-β(1–42) fibrils. Proc Natl Acad Sci 102
920 17342–17347

921 Mishra M, Raik S, Rattan V, Bhattacharyya S (2023) Mitochondria transfer as a potential
922 therapeutic mechanism in Alzheimer's disease-like pathology. Brain Res 148544

923 Mishra SK, Singh S, Shukla S, Shukla R, (2018) Intracerebroventricular streptozotocin
924 impairs adult neurogenesis and cognitive functions via regulating neuroinflammation
925 and insulin signaling in adult rats. Neurochemistry International 113, 56-68

926 Mitchell MJ, Billingsley MM, Haley RM, Wechsler ME, Peppas NA, Langer R (2021)
927 Engineering precision nanoparticles for drug delivery. Nat Rev Drug Discov 20(2),
928 101-124

929 Moghaddam AH, Zare M (2018) Neuroprotective effect of hesperetin and nano-hesperetin on
930 recognition memory impairment and the elevated oxygen stress in rat model of
931 Alzheimer's disease. Biomed Pharmacother 97, 1096-1101

932 Mosmann T (1983) Rapid colorimetric assay for cellular growth and survival: application to
933 proliferation and cytotoxicity assays, J. Immunol Methods 65, 55–63

934 Muchtaridi M, Lestari D, Khairul Ikram NK, Gazzali AM, Hariono M, Wahab HA, (2021)
935 Decaffeination and neuraminidase inhibitory activity of arabica green coffee (Coffea
936 arabica) beans: chlorogenic acid as a potential bioactive compound. Molecules 26(11),
937 3402

938 Murugan C, Rajkumar M, Kanipandian N, Thangaraj R, Vimala K, Kannan S (2020)
939 Nanoformulated CPMSN biomaterial regulates proinflammatory cytokines to heal
940 wounds and kills drug-resistant bacteria. Curr Sci 118(10), 1583

941 Ni N, Wang W, Sun Y, Sun X, Leong DT (2022) Inducible endothelial leakiness in
942 nanotherapeutic applications. Biomat 287, 121640

943 Okolie JA, Patra BR, Mukherjee A, Nanda S, Dalai AK, Kozinski JA (2021) Futuristic
944 applications of hydrogen in energy, biorefining, aerospace, pharmaceuticals and
945 metallurgy. Int J Hydrog Energy 46(13), 8885-8905

946 Oladzadabbasabadi N, Nafchi AM, Ariffin F, Wijekoon MJO, Al-Hassan AA, Dheyab MA,
947 Ghasemlou M (2022) Recent advances in extraction, modification, and application of
948 chitosan in packaging industry. Carbohydr Polym 277, 118876

949 Pan Y, Zhang Y, Liu N, Lu W, Yang J, Li Y, Liu Z, Wei Y, Lou Y, Kong J (2021) Vitamin D
950 attenuates alzheimer-like pathology induced by okadaic acid. ACS Chem Neurosci
951 12(8), 1343-1350

952 Pasieka A, Panek D, Szałaj N, Espargaro A, Więckowska A, Malawska B, Sabate R, Bajda M
953 (2021) Dual Inhibitors of Amyloid-β and Tau Aggregation with Amyloid-β
954 Disaggregating Properties: Extended In Cellulo, In Silico, and Kinetic Studies of
955 Multifunctional Anti-Alzheimer's Agents. ACS Chem Neurosci 12, 2057−2068

956 Paxinos G, Watson CR, Emson PC (1980) AChE-stained horizontal sections of the rat brain
957 in stereotaxic coordinates. J Neurosci Methods 3(2), 129-149

958 Penney J, Ralvenius WT, Tsai LH (2020) Modeling Alzheimer's disease with iPSC-derived
959 brain cells. Mol Psychiatry 25(1), 148-167

960 Rajkumar M, Sakthivel M, Senthilkumar K, Thangaraj R, Kannan S (2022a) Galantamine
961 tethered hydrogel as a novel therapeutic target for streptozotocin-induced Alzheimer's
962 disease in Wistar rats. Curr Res Pharmacol Drug Discov 3, 100100

963 Rajkumar M, Vimala K, Tamiliniyan DD, Thangaraj R, Jaganathan R, Kumaradhas P,
964 Kannan S, (2022b) Gelatin/polyvinyl alcohol loaded magnesium hydroxide
965 nanocomposite attenuates neurotoxicity and oxidative stress in Alzheimer's disease
966 induced rats. Int J Biol Macromol 222, 2122-2143

967 Ramagiri S, Taliyan R (2017) Remote limb ischemic post conditioning during early
968 reperfusion alleviates cerebral ischemic reperfusion injury via GSK-3β/CREB/BDNF
969 pathway. Eur J Pharmacol 803, 84-93

970 S. Jokara M, Erfanib O, Bavic S, Khazaeid M, Sharifzadehe M, Hajiramezanalia D, Beikif A,
971 Shamloog (2020) Design of peptide-based inhibitor agent against amyloid-β

aggregation: Molecular docking, synthesis and in vitro evaluation. Bioorg Chem 102, 104050

Saez-Orellana F, Godoy PA, Bastidas CY, Silva-Grecchi T, Guzmán L, Aguayo LG, Fuentealba J (2016) ATP leakage induces P2XR activation and contributes to acute synaptic excitotoxicity induced by soluble oligomers of β-amyloid peptide in hippocampal neurons. Neuropharmacol 100, 116-123

Sahu T, Ratre YK, Chauhan S, Bhaskar LVKS, Nair MP, Verma HK (2021) Nanotechnology based drug delivery system: Current strategies and emerging therapeutic potential for medical science. J Drug Deliv Sci Technol 63, 102487

Sharma S, Taliyan R (2015) Synergistic effects of GSK-3β and HDAC inhibitors in intracerebroventricular streptozotocin-induced cognitive deficits in rats. Naunyn Schmiedebergs Arch Pharmacol 388, 337-349

Silva AA, Sousa AMF, Furtado CR, Carvalho N.M (2022) Green magnesium oxide prepared by plant extracts: synthesis, properties and applications. Mater Today Sustain 100203

Sottocasa GL, Kuylenstierna BO, Ernster L, Bergstrand A (1967) An electron-transport system associated with the outer membrane of liver mitochondria: a biochemical and morphological study. J Cell Biol 32(2), 415-438

Taheri F, Joushi S, Esmaeilpour K, Sheibani V, Ebrahimi MN, Taheri Zadeh Z, (2023) Music alleviates cognitive impairments in an animal model of autism. Int J Dev Neurosci

Tramutola A, Arena A, Cini C, Butterfield DA, Barone E (2017) Modulation of GLP-1 signaling as a novel therapeutic approach in the treatment of Alzheimer's disease pathology. Expert Rev Neurother 17(1), 59-75

994 Ucar A, Özgeriş FB, Parlak V, Yeltekin AÇ, Kocaman EM, Alak G, Atamanalp M (2022)
995 Neurotoxic responses of rainbow trout (Oncorhynchus mykiss) exposed to fipronil:
996 multi-biomarker approach to illuminate the mechanism in brain. Drug Chem Toxicol
997 45(5), 2140-2145

998 Varesi A, Campagnoli LIM, Carrara A, Pola I, Floris E, Ricevuti G, Chirumbolo S, Pascale A
999 (2023) Non-enzymatic antioxidants against Alzheimer's disease: prevention, diagnosis
1000 and therapy. Antioxidants 12(1), 180

1001 Verma V, Singh D, Kh R (2020) Sinapic acid alleviates oxidative stress and neuro-
1002 inflammatory changes in sporadic model of Alzheimer's disease in rats. Brain Sci
1003 10(12), 923

1004 Wills E (1966) Mechanisms of lipid peroxide formation in animal tissues. Biochem J 99 667

1005 Xiang X, Wang X, Wu Y, Hu J, Li Y, Jin S, Wu X (2022) Activation of GPR55 attenuates
1006 cognitive impairment, oxidative stress, neuroinflammation, and synaptic dysfunction in
1007 a streptozotocin-induced Alzheimer's mouse model. Pharmacol Biochem Behav 214,
1008 173340

1009 Yamini P, Ray RS, Chopra K (2018) Vitamin D 3 attenuates cognitive deficits and
1010 neuroinflammatory responses in ICV-STZ induced sporadic Alzheimer's disease.
1011 Inflammopharmacol 26, 39-55

1012 Yamini P, Ray RS, Yadav S, Dhaliwal J, Yadav M, Kondepudi KK, Chopra K (2022)
1013 α7nAChR activation protects against oxidative stress, neuroinflammation, and central
1014 insulin resistance in ICV-STZ-induced sporadic Alzheimer's disease. Pharmacology
1015 Biochem Behav 217, 173402

Yin Z, Gao D, Du K, Han C, Liu Y, Wang Y, Gao X (2022) Rhein Ameliorates Cognitive Impairment in an APP/PS1 transgenic mouse model of Alzheimer's disease by relieving oxidative stress through activating the SIRT1/PGC-1α pathway. Oxid Med Cell Longev

Zarrintaj P, Ramsey JD, Samadi A, Atoufi Z, Yazdi M.K, Ganjali MR, Amirabad LM, Zangene E, Farokhi M, Formela K, Saeb MR (2020) Poloxamer: A versatile tri-block copolymer for biomedical applications. Acta biomater 110, 37-67

Zhou M, Chen S, Peng P, Gu Z, Yu J, Zhao G, Deng Y, (2019) Dulaglutide ameliorates STZ induced AD-like impairment of learning and memory ability by modulating hyperphosphorylation of tau and NFs through GSK3β. Biochem Biophys Res Commun 511(1), 154-160

Zhuang Y, Cui W, (2021) Biomaterial-based delivery of nucleic acids for tissue regeneration. Adv Drug Deliv Rev 176, 113885

Table 1: Effect of CH/PLA/MgONCs treatment on oxidative stress markers in different brain regions (cortex and hippocampus). The analysis of data was done by using one-way ANOVA followed by Tukey's post hoc test for multiple comparisons. All the values were shown as mean ± SD. $^{\#\#}p < 0.01$, $^{\#\#\#}p < 0.001$ compared with control group and $^{*}p < 0.05$, $^{**}p < 0.01$, $^{***}p < 0.0001$ compared with ICV-STZ-treated group.

Treatment group	Brain region	MDA (nM/mg protein)	Nitrite (µg of nitrite/mg protein)	PCO (nM/mg protein)
Control	Cortex	2.98 ± 0.75	125.83 ± 5.38	15.39 ± 1.83
	Hippocampus	4.37 ± 0.83	167.56 ± 8.23	26.82 ± 3.29
ICV-STZ (3mg/kg)	Cortex	6.83 ± 0.91$^{\#\#\#}$	201.59 ± 8.23$^{\#}$	34.24 ± 2.73$^{\#\#}$
	Hippocampus	8.42 ± 1.02$^{\#\#}$	263.84 ± 7.90$^{\#\#\#}$	47.39 ± 2.45$^{\#\#\#}$
STZ+CH	Cortex	5.26 ± 0.82**	182.65 ± 6.94***	29.46 ± 2.63
(10mg/kg)	Hippocampus	7.13 ± 1.53*	239.57 ± 7.35**	41.73 ± 1.98**
STZ+MgO	Cortex	4.28 ± 0.72**	171.48 ± 5.48*	24.38 ± 2.18***
(10mg/kg)	Hippocampus	6.46 ± 1.49**	196.73 ± 4.93**	32.39 ± 1.56**
STZ+CH/MgO	Cortex	3.71 ± 0.63***	148.36 ± 4.78***	20.93 ± 1.83***
(10-mg/kg)	Hippocampus	5.92 ± 1.85**	184.69 ± 5.86**	25.76 ± 1.48*
STZ+CH/PLA/ MgONCs (10mg/kg)	Cortex	3.18 ± 0.57	136.87 ± 4.28	17.29 ± 1.26
	Hippocampus	4.64 ± 1.38	175.78 ± 5.37	20.63 ± 1.75

Table 2: Effect of CH/PLA/MgONCs treatment on mitochondrial respiratory enzyme complexes in different brain regions (cortex and hippocampus). The analysis of data was done by using one-way ANOVA followed by Tukey's post hoc test for multiple comparisons. All the values were shown as mean ± SD. $^{\#\#}p < 0.01$, $^{\#\#\#}p < 0.0001$ compared with control group and $^{*}p < 0.05$, $^{**}p < 0.01$, $^{***}p < 0.0001$ compared with ICV-STZ-treated group.

Treatment group	Brain region	Mitochondrial complexes I-activity (nM of NADH oxidized/min/ mg protein)	Mitochondrial complexes II-activity (nM of substrate/min/ mg protein)	Mitochondrial complexes III-activity (No. of viable cell (% of control)	Mitochondrial complexes IV-activity (nM cyt-c oxidized/min/ mg protein)
Control	Cortex	92.57 ± 4.78	176.3 ± 7.51	119.3 ± 5.29	135.4 ± 5.35
	Hippocampus	121.7 ± 5.86	206.7 ± 8.57	165.4 ± 6.39	154.5 ± 6.87
ICV-STZ (3mg/kg)	Cortex	39.68 ± 2.95$^{\#\#}$	94.71 ± 4.58$^{\#\#}$	65.59 ± 3.96$^{\#\#\#}$	72.90 ± 3.48$^{\#\#}$
	Hippocampus	65.84 ± 4.80$^{\#\#\#}$	124.7 ± 5.18$^{\#}$	89.88 ± 3.90$^{\#\#}$	90.43 ± 3.64$^{\#\#\#}$
STZ+CH	Cortex	45.64 ± 3.46***	109.2 ± 4.98***	78.51 ± 4.37**	89.38 ± 3.99*
(10mg/kg)	Hippocampus	74.94 ± 4.12**	149.3 ± 5.13**	107.4 ± 4.97***	102.5 ± 4.17***
STZ+MgO	Cortex	58.29 ± 4.10*	124.9 ± 6.15*	87.39 ± 4.28*	107.9 ± 4.55**
(10-mg/kg)	Hippocampus	88.54 ± 3.87***	166.8 ± 5.98***	125.7 ± 4.76**	125.8 ± 5.11*
STZ+CH/ MgO (10mg/kg)	Cortex	76.80 ± 5.78*	139.6 ± 5.39**	98.39 ± 5.08***	118.7 ± 4.33**
	Hippocampus	97.96 ± 5.12*	182.9 ± 6.27**	144.6 ± 5.98***	137.2 ± 6.22***
STZ+CH/PLA/ MgO (10mg/kg)	Cortex	84.81 ± 5.90	156.3 ± 6.15	116.2 ± 6.89	127.3 ± 5.26
	Hippocampus	109.7 ± 6.12	196.5 ± 7.62	159.5 ± 7.55	148.6 ± 6.12

Figure legends:

Fig. 1. UV-Vis spectrophotometer analyses of CH/PLA/MgONCs are shown in the absorption value Fig. (A). The FT-IR spectra of CH/PLA/MgONCs indicate the presence of different functional groups (B). The swelling properties of CH, MgO, CH/MgO, and CH/PLA/MgONCs as shown in Fig. C. The drug release properties of CH/PLA/MgONCs as shown in Fig. (D).

Fig. 2. SEM-EDAX analysis of synthesized CH/PLA/MgONCs (A), spectrum analysis (B), and elemental mapping analysis (C).

Fig. 3. The experimental schematic diagram for drug dosing and therapeutic evaluation of CH/PLA/MgONCs.

Fig. 4. CH/PLA/MgONCs effects on the MWM task for swimming schematic diagram (A), mean escape latency (B), time spent in the target quadrant where the platform is located (C) platform crossing time (D) and error time (E). Acquisition data is presented in the bar chart (mean ± SD) and was analyzed by two-way ANOVA followed by Bonferroni's post hoc test for multiple comparisons (n = 6). $^{\#\#}p < 0.01$ and $^{\#\#\#}p < 0.001$ versus the control group, and $^{*}p < 0.05$, $^{**}p < 0.01$ and $^{***}p < 0.001$ versus the ICV-STZ treated group.

Fig. 5. CH/PLA/MgONCs effects on the PA task (A) and Y-maze test (B). Acquisition data is presented in the bar chart (mean ± SD) and was analyzed by two-way ANOVA followed by Bonferroni's post hoc test for multiple comparisons (n = 6). $^{\#\#}p < 0.01$ and $^{\#\#\#}p < 0.001$ versus the control group, and $^{*}p < 0.05$, $^{**}p < 0.01$ and $^{***}p < 0.001$ versus the ICV-STZ treated group.

Fig. 6. CH/PLA/MgONCs effects on the A) AChE, B) SOD, C) CAT, and D) GSH activity in the cortex and hippocampus regions for the experimental group of rats. Acquisition data was presented in the bar chart (mean ± SD) and analyzed by one-way ANOVA followed by

Tukey's post hoc test for multiple comparisons (n = 6). $^{\#\#}p < 0.01$ and $^{\#\#\#}p < 0.001$ versus the control group, and $^{*}p < 0.05$, $^{**}p < 0.01$ and $^{***}p < 0.001$ versus the ICV-STZ treated group.

Fig. 7. CH/PLA/MgONCs effects on the A) TNF-α, B) IL-6, and C) CRP activity in the hippocampus of rats in the control and experimental groups. Acquisition data is presented in the bar chart (mean ± SD) and was analyzed by one-way ANOVA followed by Tukey's post hoc test for multiple comparisons (n = 6). $^{\#\#}p < 0.01$ and $^{\#\#\#}p < 0.001$ versus the control group, and $^{*}p < 0.05$, $^{**}p < 0.01$ and $^{***}p < 0.001$ versus the ICV-STZ treated group.

Fig. 8. Effects of CH/PLA/MgONCs effects on the histopathological changes with hematoxylin and eosin staining of vital organs such as the brain, heart, liver, kidney, and lung for experimental rats (scale bar: 50 μm).

Fig. 9. 3D intermolecular interactions of CA plant major phytochemical of (A) Caffeic acid, (B) Dihydro benzoic acid, (C) Ferulic acid, and (D) Epirosmanol binding with Aβ (protein) expression from molecular docking.

Fig.1.

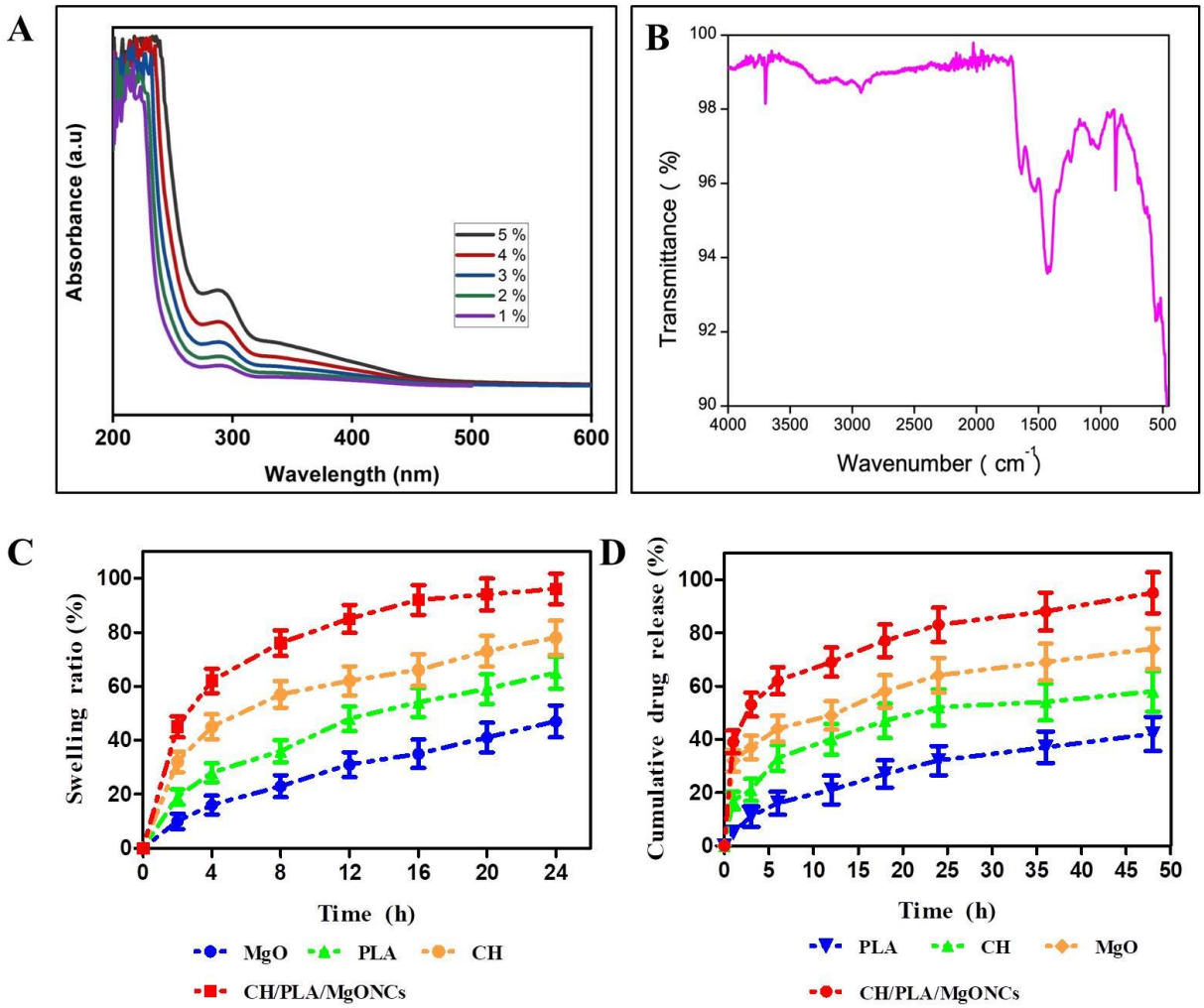
A
Absorbance (a.u)
Wavelength (nm)
5 %
4 %
3 %
2 %
1 %
B
Transmittance (%)
Wavenumber (cm-1)
C
Swelling ratio (%)
Time (h)
MgO
PLA
CH
CH/PLA/MgONCs
D
Cumulative drug release (%)
Time (h)
PLA
CH
MgO
CH/PLA/MgONCs

Fig. 2.

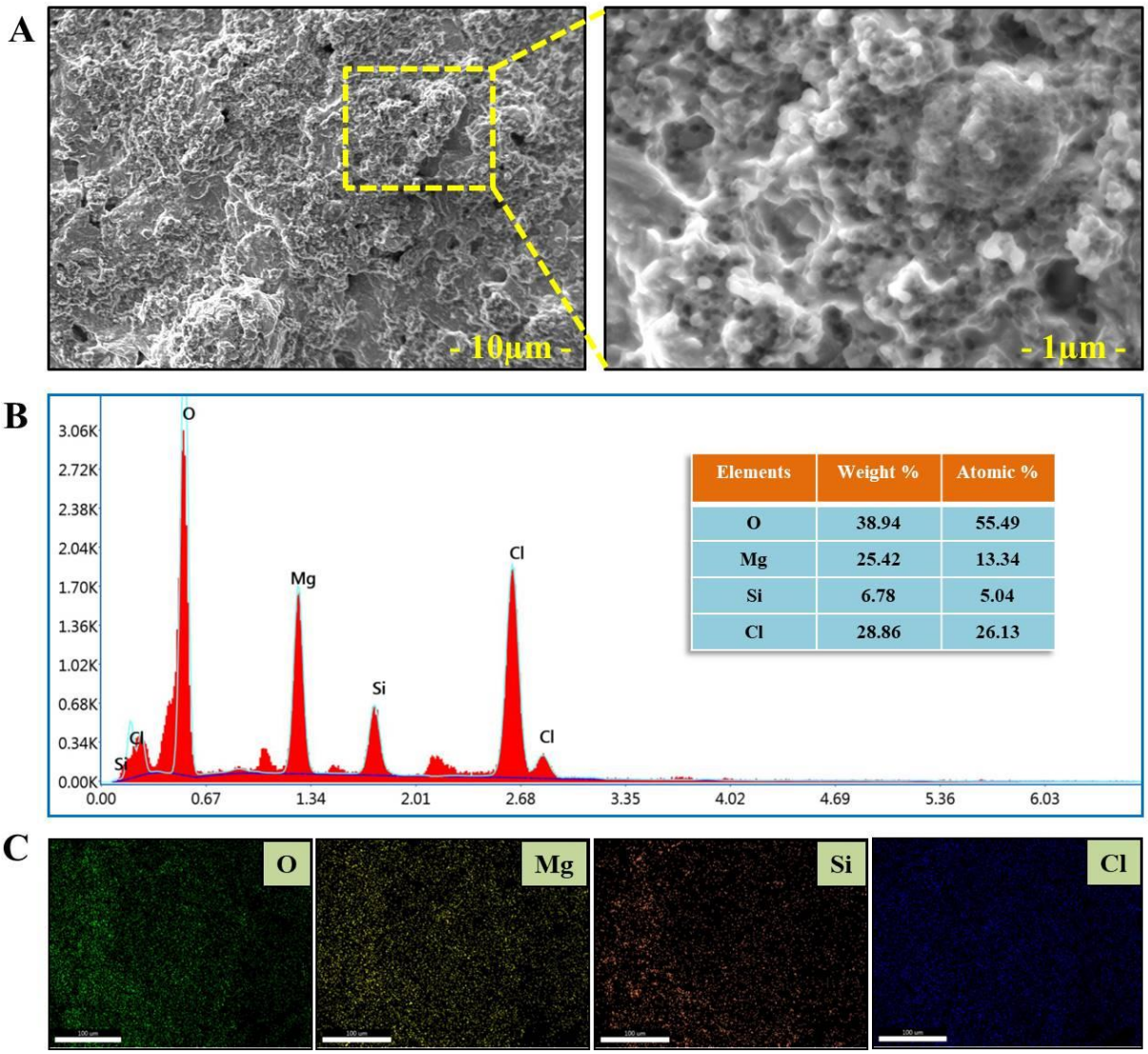
A
- 10µm -
- 1µm -
B
3.06K
2.72K
2.38K
2.04K
1.70K
1.36K
1.02K
0.68K
0.34K
0.00K
0.00
0.67
1.34
2.01
2.68
3.35
4.02
4.69
5.36
6.03
O
Mg
Si
Cl
Cl
Cl
Si
Elements | Weight % | Atomic %
O | 38.94 | 55.49
Mg | 25.42 | 13.34
Si | 6.78 | 5.04
Cl | 28.86 | 26.13
C
O
Mg
Si
Cl

Fig. 3.

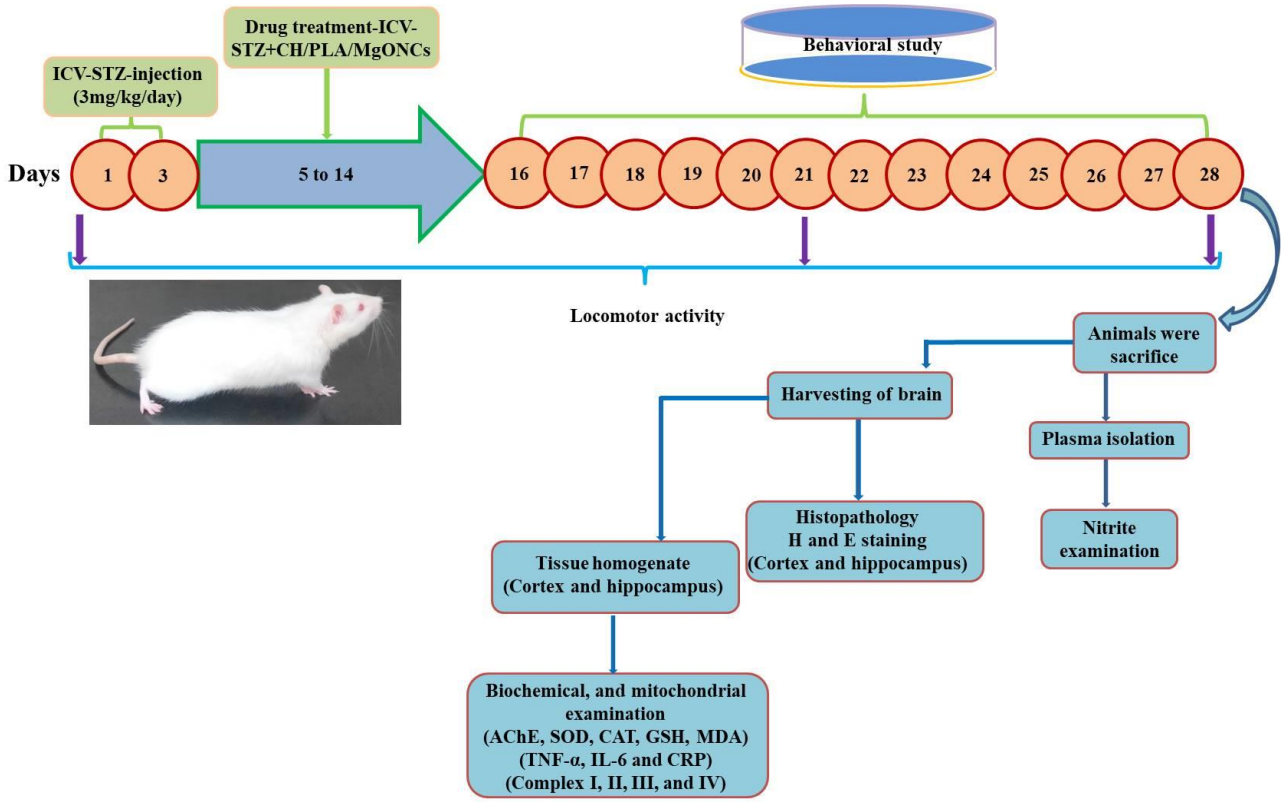
Drug treatment-ICV-STZ+CH/PLA/MgONCs
ICV-STZ-injection (3mg/kg/day)
Behavioral study
Days
1
3
5 to 14
16
17
18
19
20
21
22
23
24
25
26
27
28
Locomotor activity
Animals were sacrifice
Harvesting of brain
Plasma isolation
Histopathology H and E staining (Cortex and hippocampus)
Nitrite examination
Tissue homogenate (Cortex and hippocampus)
Biochemical, and mitochondrial examination (AChE, SOD, CAT, GSH, MDA) (TNF-α, IL-6 and CRP) (Complex I, II, III, and IV)

Fig. 4.

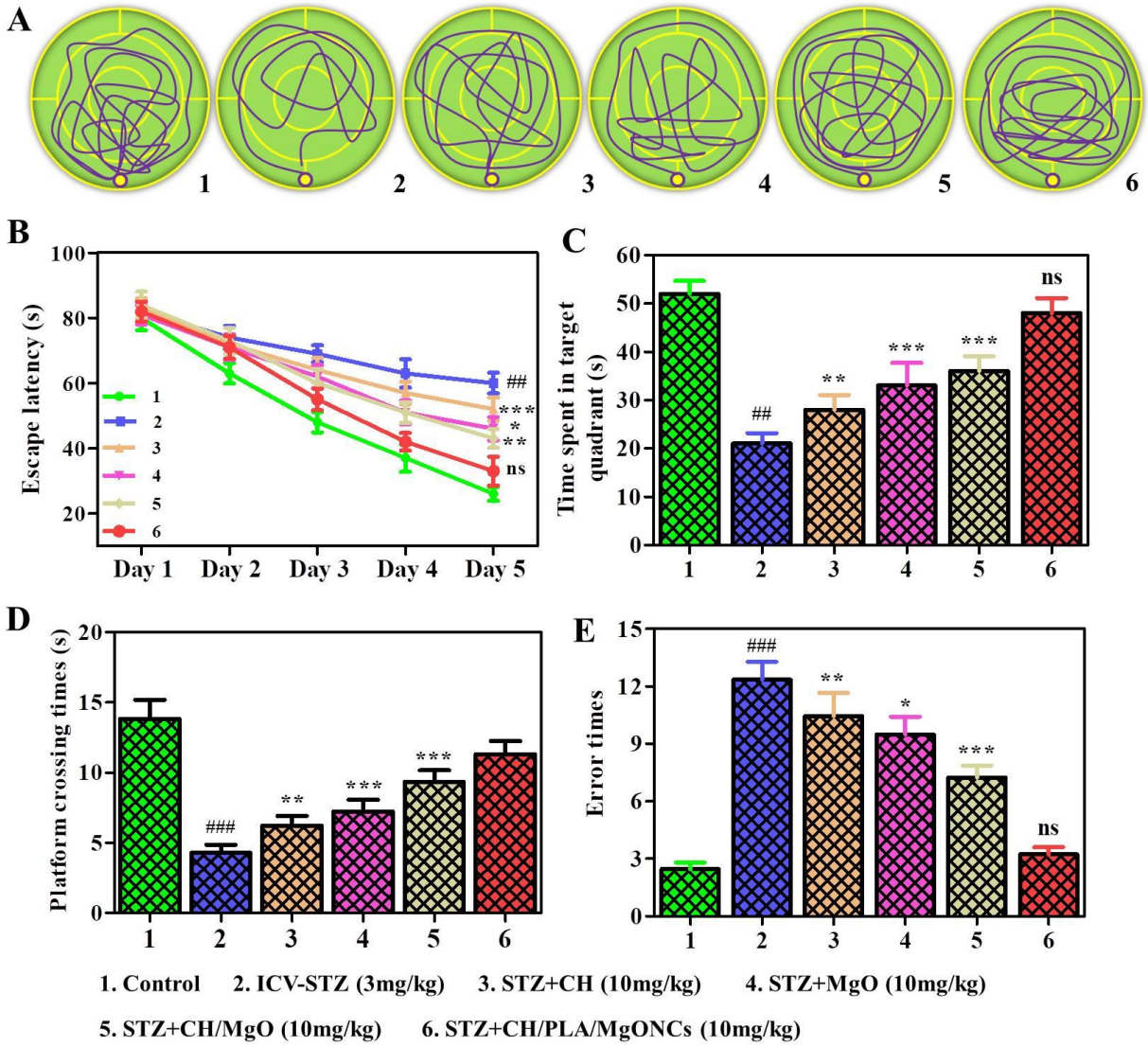
A
1
2
3
4
5
6
B
Escape latency (s)
Day 1
Day 2
Day 3
Day 4
Day 5
##
***
*
**
ns
C
Time spent in target quadrant (s)
ns
D
Platform crossing times (s)
###
E
Error times
1. Control
2. ICV-STZ (3mg/kg)
3. STZ+CH (10mg/kg)
4. STZ+MgO (10mg/kg)
5. STZ+CH/MgO (10mg/kg)
6. STZ+CH/PLA/MgONCs (10mg/kg)

Fig. 5.

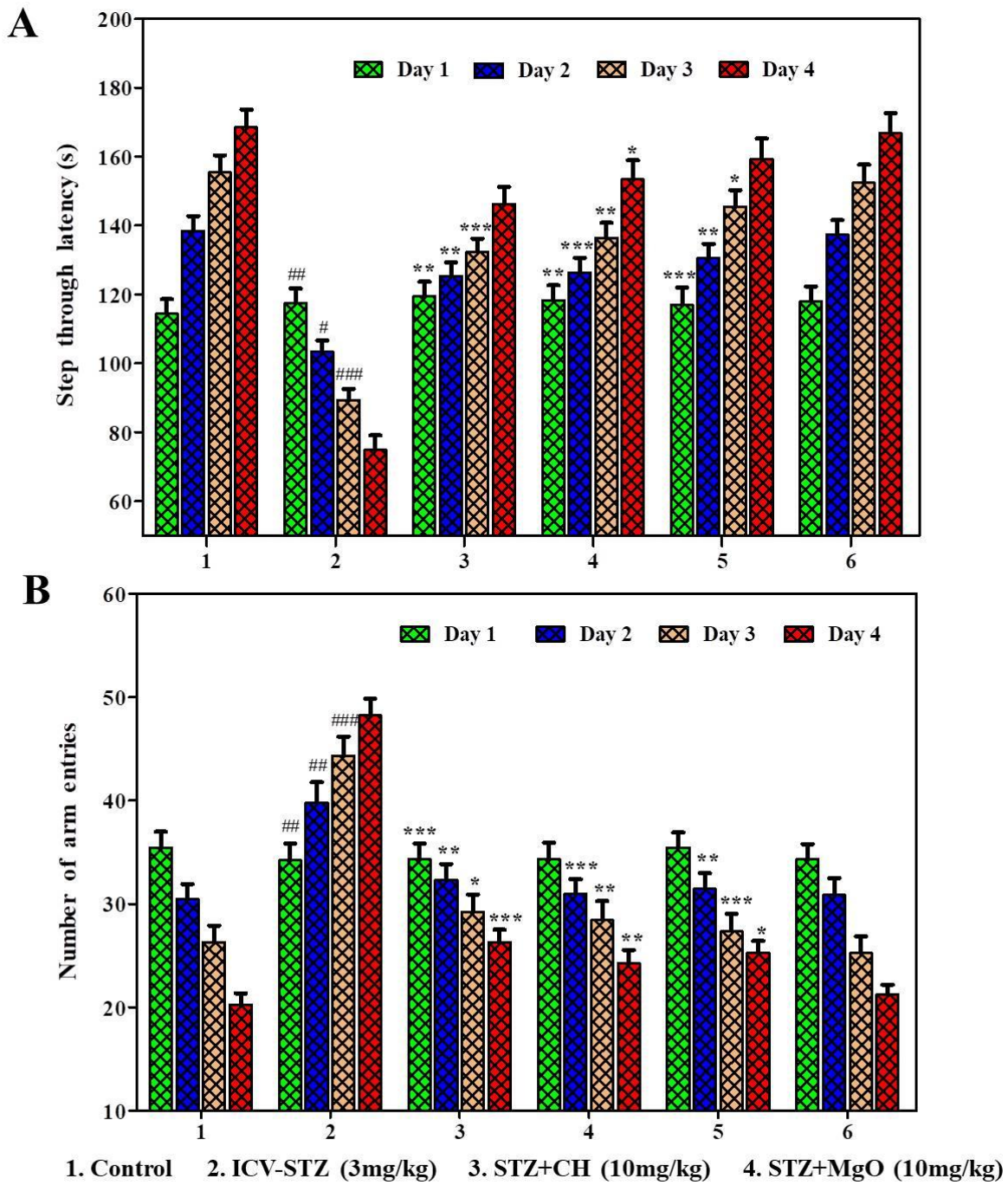
A
Step through latency (s)
Day 1
Day 2
Day 3
Day 4
B
Number of arm entries
1. Control
2. ICV-STZ (3mg/kg)
3. STZ+CH (10mg/kg)
4. STZ+MgO (10mg/kg)
5. STZ+CH/MgO (10mg/kg)
6. STZ+CH/PLA/MgONCs (10mg/kg)

Fig. 6.

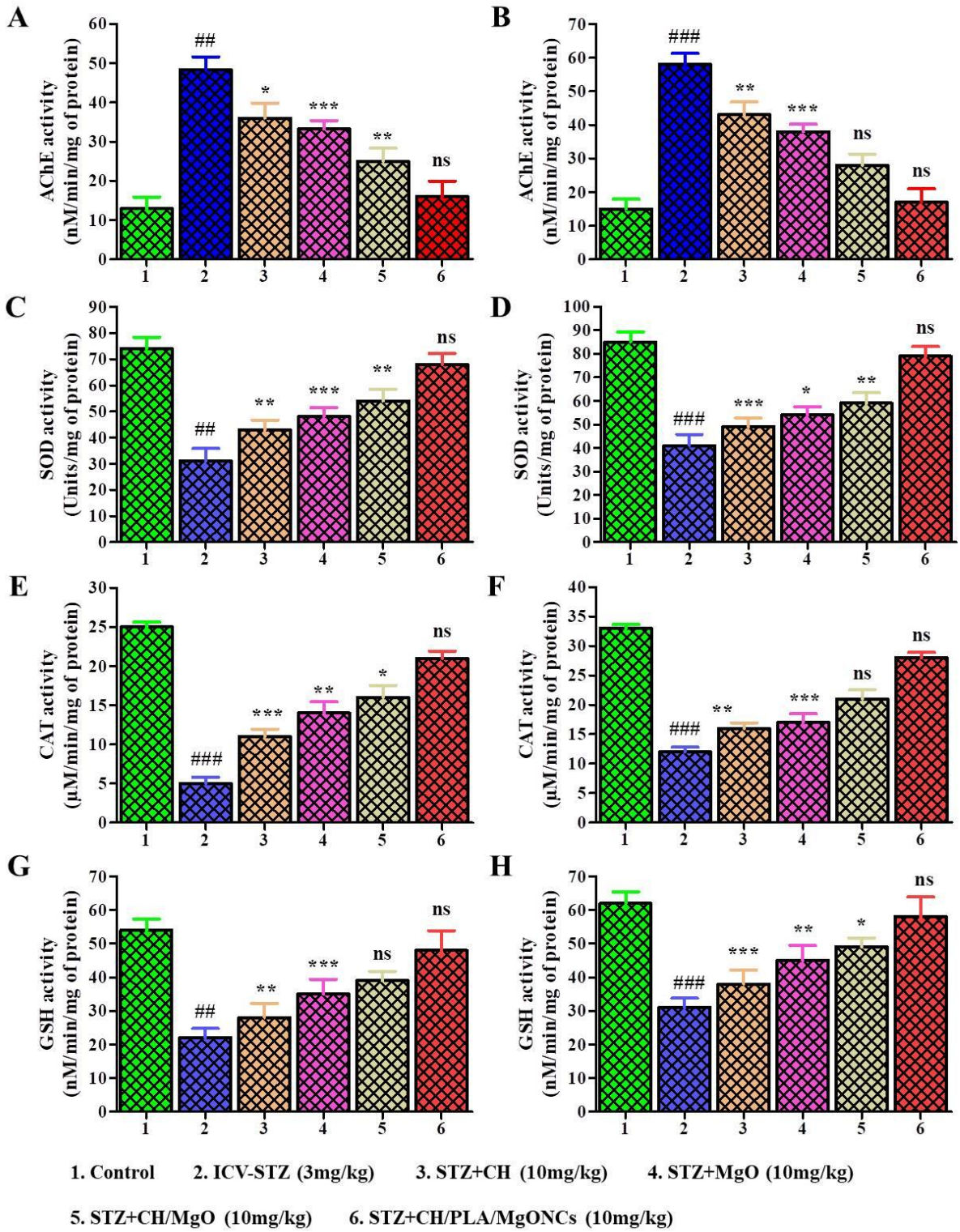
A
AChE activity (nM/min/mg of protein)
B
AChE activity (nM/min/mg of protein)
C
SOD activity (Units/mg of protein)
D
SOD activity (Units/mg of protein)
E
CAT activity (µM/min/mg of protein)
F
CAT activity (µM/min/mg of protein)
G
GSH activity (nM/min/mg of protein)
H
GSH activity (nM/min/mg of protein)
1. Control
2. ICV-STZ (3mg/kg)
3. STZ+CH (10mg/kg)
4. STZ+MgO (10mg/kg)
5. STZ+CH/MgO (10mg/kg)
6. STZ+CH/PLA/MgONCs (10mg/kg)

Fig. 7.

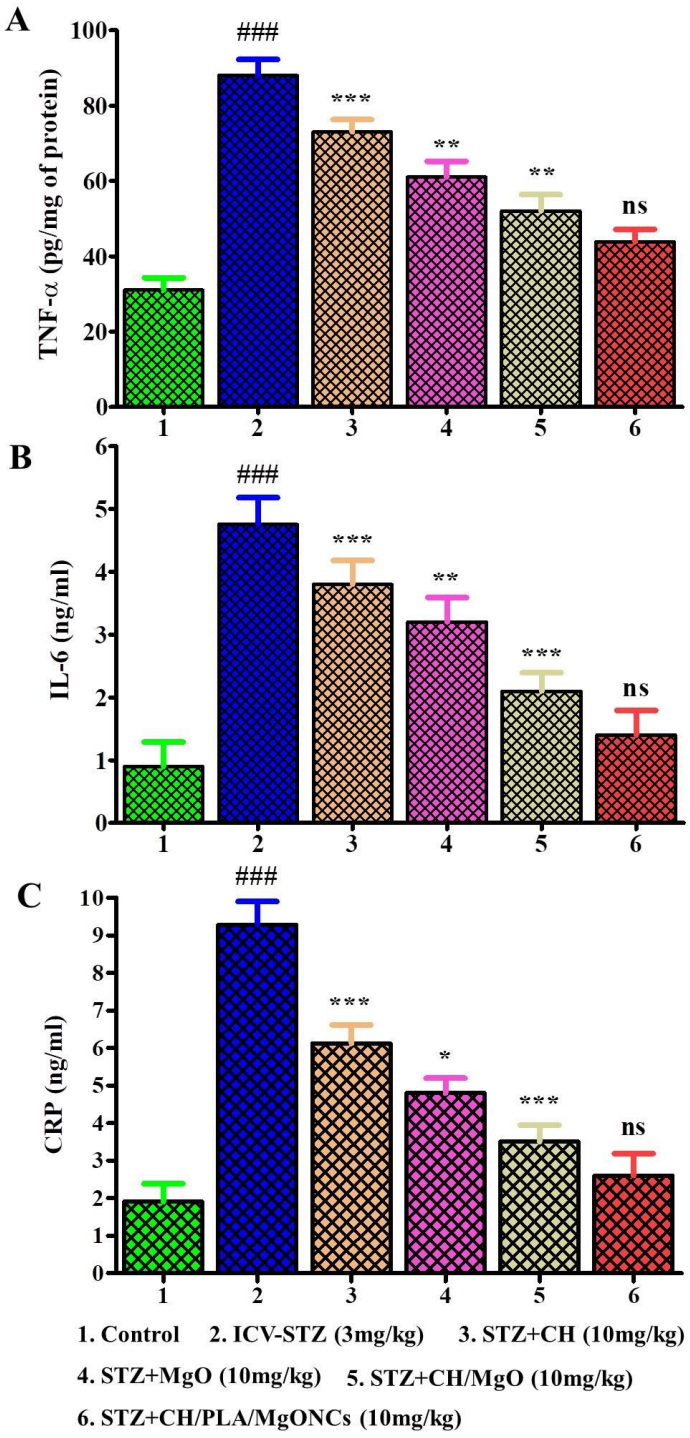
A
TNF-α (pg/mg of protein)
100
80
60
40
20
0
###
***
**
**
ns
1
2
3
4
5
6
B
IL-6 (ng/ml)
6
5
4
3
2
1
0
###
***
**
***
ns
1
2
3
4
5
6
C
CRP (ng/ml)
10
9
8
7
6
5
4
3
2
1
0
###
***
*
***
ns
1
2
3
4
5
6
1. Control
2. ICV-STZ (3mg/kg)
3. STZ+CH (10mg/kg)
4. STZ+MgO (10mg/kg)
5. STZ+CH/MgO (10mg/kg)
6. STZ+CH/PLA/MgONCs (10mg/kg)

Fig. 7.

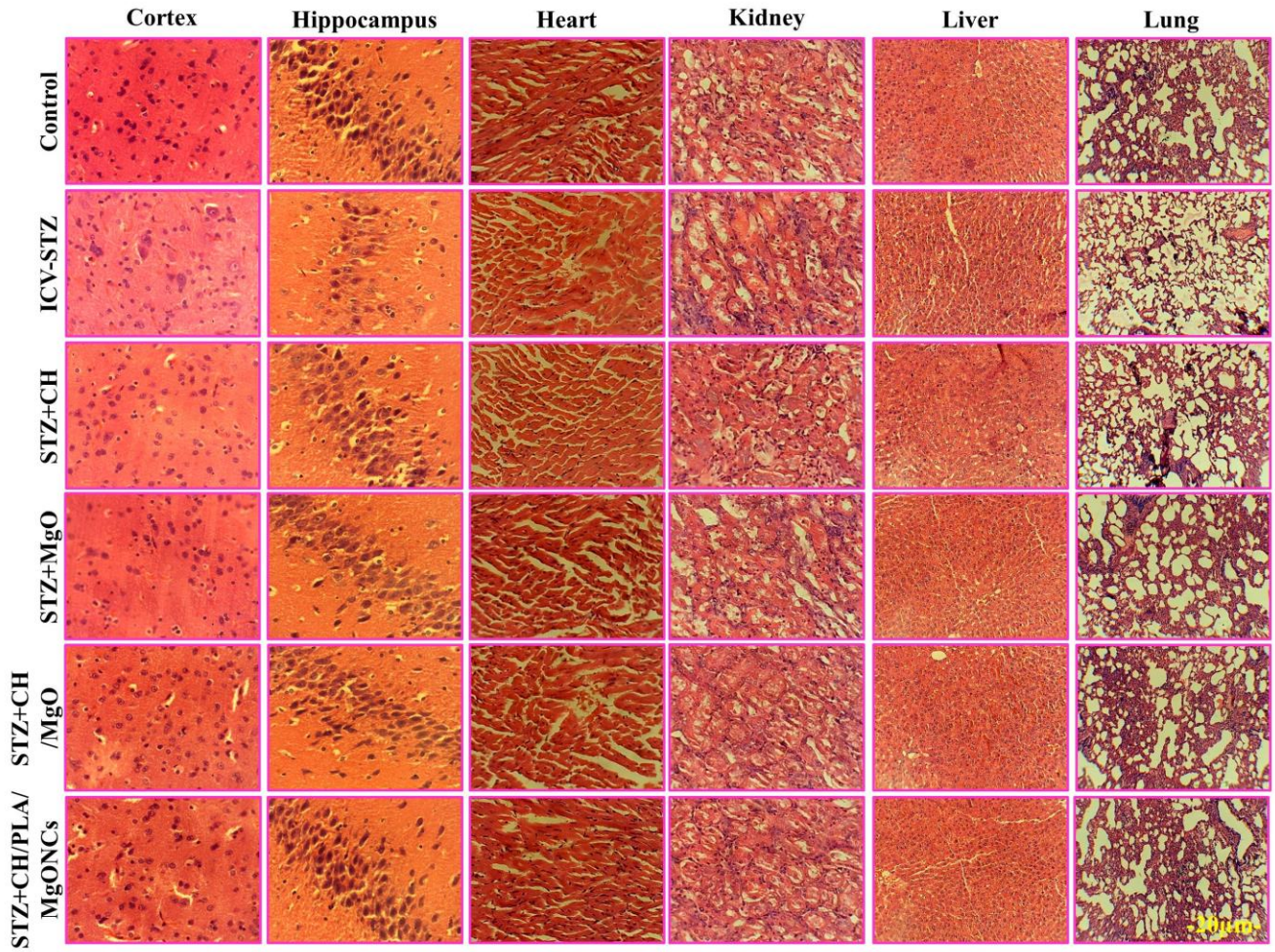
Cortex
Hippocampus
Heart
Kidney
Liver
Lung
Control
ICV-STZ
STZ+CH
STZ+MgO
STZ+CH /MgO
STZ+CH/PLA/ MgONCs

Fig. 9.

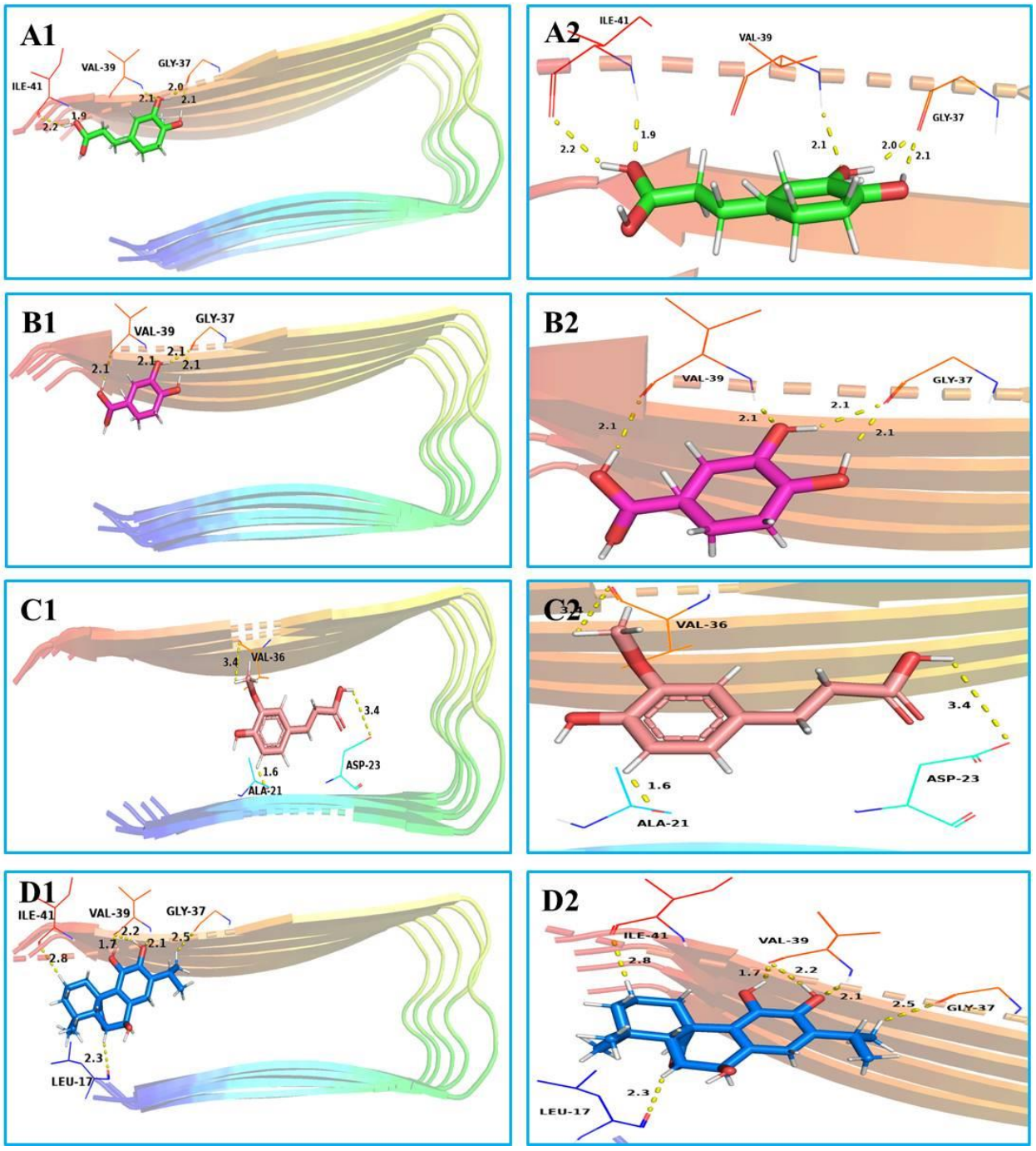

1174

1175

1176